LARGE-SCALE STREAMWISE TURBULENT STRUCTURES IN HYPERSONIC BOUNDARY LAYERS

A Thesis

by

BENJAMIN L. ENGLISH

Submitted to the Office of Graduate Studies of
Texas A&M University
in partial fulfillment of the requirements for the degree of

MASTER OF SCIENCE

Approved by:

Chair of Committee,	Rodney Bowersox
Co-Chair of Committee,	Edward White
Committee Member,	Simon North
Head of Department,	Rodney Bowersox

May 2013

Major Subject: Aerospace Engineering

ABSTRACT

Prior research in the field of boundary layer turbulence has identified streamwise-elongated large-scale turbulence structures in both low speed compressible and high speed ($M = 2.0$) flow. No experimental work has been done in any flow of $M \geq 3$ in an attempt to identify the presence or quantify the behavior of these structures, nor has any study of favorable pressure gradient or surface roughness element effects on these structures been conducted. This research used high-resolution Particle Imaging Velocimetry in a $M = 4.9$ blow-down wind tunnel accompanied by a series of data analysis in order to identify the existence of streamwise-elongated large-scale turbulence structures in a hypersonic boundary layer. Furthermore, this study identified physical and statistical behavior which suggests that increasing favorable pressure gradient had a substantial impact on both the structural coherence and relative intensity of these turbulent structures at all boundary layer heights tested. This experiment also identified similar effects on these structures in the lower half of the boundary layer as a result of the introduction of surface roughness elements. Finally, several trends were identified between the averaged turbulence statistics and the behavior of the large-scale streamwise-elongated turbulence structures present in this study.

DEDICATION

I would like to dedicate this work to my parents, Ben and Cathy English. I owe my motivation, persistence, and love of learning to their tireless work and constant guidance during my upbringing. They have also been quick to listen and provide advice and support throughout my time in higher education. My accomplishments are nothing more than a reflection of their excellent parenting. They ensured that I had the best educational and character development possible as a child, and that is one of the greatest gifts that anyone could ever ask for.

I would also like to dedicate this work to all Marines, past and present. Many men and women have stood their time as guardians on the wall, and I only hope that I can live up to their legacy through my service to Corps and Country.

ACKNOWLEDGEMENTS

The work presented in this thesis would not be possible without the generous support and assistance of many others. First and foremost, I would like to thank my Research Advisor and Committee Chair, Dr. Rodney Bowersox, for providing me the great opportunity and much of the necessary funding to achieve this step in my academic career. Without his constant support and guidance, the completion of this thesis and the research that it was based upon would not have been possible.

I would also like to thank the United States Marine Corps for allowing me the time off during my career and necessary financial support to complete this endeavor.

The help and guidance provided by Scott Peltier and Dr. Ray Humble have been indispensable in the completion of this work. Scott helped greatly in the initial setup and design of this experiment. He has also been completely open in sharing his data and findings to help complete and emphasize my own. Dr. Humble was a source of inspiration and both conceptual and technical knowledge throughout the project, and his assistance during the writing and proofreading of this work was both crucial and greatly appreciated. Furthermore, I would like to thank all of the members of the National Aerothermochemistry Lab Team for their guidance and support, particularly in tunnel and compressor maintenance, without which this thesis would not have been possible.

Finally, I would like to thank my family and friends. Without their constant support, I would not have been able to even begin this work, much less see it through to completion.

NOMENCLATURE

PIV	Particle Imaging Velocimetry
RZPG	Roughness Element Zero Pressure Gradient
SPG	Strong Pressure Gradient
TiO_2	Titanium Dioxide
TKE	Turbulent Kinetic Energy
WPG	Weak Pressure Gradient
ZPG	Zero Pressure Gradient
M	Mach Number
R_e	Reynolds Number
R_{ux}	Streamwise Autocorrelation of the *U*-velocity
R_{uz}	Spanwise Autocorrelation of the *U*-velocity
R_{wx}	Streamwise Correlation of the *W*-velocity
R_{wz}	Spanwise Correlation of the *W*-velocity
S_t	Stokes Number
U	Streamwise Velocity
$U_{3\sigma}$	3-sigma Averaged Streamwise Velocity
U_{ref}	Reference Velocity
U_{xz}	Local Instantaneous Velocity at Location x, z
U_∞	Free-stream Velocity
W	Spanwise Velocity

$W_{3\sigma}$	3-sigma Averaged Spanwise Velocity
X	Global Streamwise Axis
Y	Global Wall-normal Axis
h	Height
u_τ	Skin-friction Velocity
u'_{RMS}	Root Mean Square of Fluctuating Streamwise Velocity
$\overline{u'u'}$	*uu* Component of the Reynolds Shear Stress
$\overline{u'w'}$	*uw* Component of the Reynolds Shear Stress
w'_{RMS}	Root Mean Square of Fluctuating Spanwise Velocity
$\overline{w'w'}$	*ww* Component of the Reynolds Shear Stress
x	Local Streamwise Axis
y	Local Wall-normal Axis
z	Spanwise Axis
$\Delta\varepsilon_{var}$	Change in ε_{var}
δ	Boundary Layer Height
ε_{var}	Variable
η	Statistical Uncertainty Coefficient
τ_p	Particle Response Time
τ_f	Flow Response Time
ω	Reynolds Shear Stress Correlation Coefficient

TABLE OF CONTENTS

LIST OF FIGURES

LIST OF TABLES

CHAPTER I

INTRODUCTION AND RESEARCH OBJECTIVES

A. Turbulent Boundary Layer Overview

A boundary layer is a fluid flow region adjacent to the surface of a body in motion where the velocity of the fluid increases from zero at the objects surface to the free stream velocity some distance away from the surface. This feature is a result of the no-slip condition of fluid dynamics, which requires that at the immediate surface of any object in motion, the local fluid velocity must be equal to that of the object. In reality, this only happens on a molecularly thin region of the lower boundary layer. From that layer up, the streamwise velocity of the fluid, U, rapidly accelerates to meet the free stream velocity, U_∞. The boundary layer height, δ, is typically defined as the distance from the surface to the height at which $U = 0.99U_\infty$.

Every object in motion through a fluid has a boundary layer: from automobiles and aircraft, to airborne projectiles and underwater torpedoes. However, not all boundary layers have the same properties. There are two major types of boundary layers: laminar and turbulent. The leading edge of a surface begins to develop a laminar boundary layer as soon as it encounters a velocity differential with the surrounding fluid. In a laminar boundary layer, U increases towards U_∞ as the boundary layer height increases, and momentum and heat transfer exchange take place purely on a molecular level. This process can be thought of as a stack of horizontal streamlines, where each streamline has a greater velocity than the one directly beneath it. However, with increased distance

from the leading edge, increasing Reynolds number, R_e, or a change in pressure gradient, the boundary layer can quickly become turbulent. In a turbulent boundary layer, instantaneous velocity fluctuations brought on by random vorticity in the flow drive the momentum and heat transfer from the free-stream fluid to the surface, or vice versa. In a turbulent boundary layer, the change in average streamwise velocity versus height perpendicular to the surface, $\frac{\partial U}{dy}$, is much greater near the surface than that found in an equivalent laminar boundary layer. Again, this is driven by the fact that wall perpendicular velocity fluctuations within the turbulent boundary layer make the transfer of momentum happen much more rapidly than found in the laminar regime. Figure 1 shows an example of the different velocity profiles found in a laminar and turbulent boundary layer.

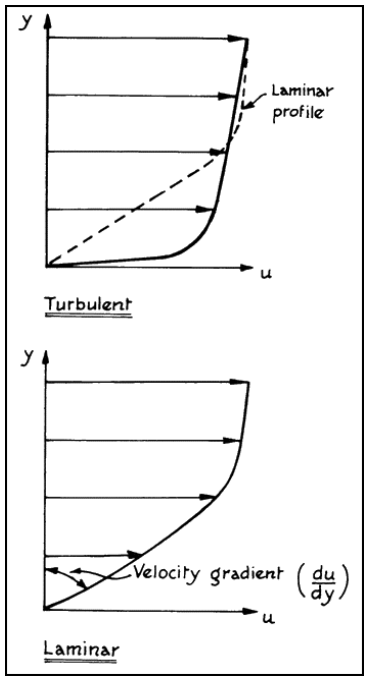

Fig. 1: Typical laminar and turbulent boundary layer profiles. Figure taken from Ref. [1].

Random vorticial structures are the base means by which mass, momentum, and energy are transported throughout the turbulent boundary layer. The size of these turbulent structures can range from structure sizes on the order of δ to structures sizes small enough to dissipate turbulent kinetic energy into heat. These structures are not intrinsically three-dimensional in nature. Even though their distribution is seemingly random, their presence can cause a fluid hysteresis which can often last for a length of many δ in the streamwise direction. The understanding of how these structures form, propagate, and dissipate within the boundary layer, as well as how they react to changes in the boundary layer itself, is crucial to the understanding of turbulent boundary layers.

B. Motivation

Although boundary layers form as laminar near the leading edge of the surface, real-world conditions such as surface roughness and shape, high R_e, and the great length of most surfaces compared to δ, cause the rapid onset of turbulence in many boundary layers. As such, the majority of any surface travelling through the atmosphere is more than likely encompassed by a turbulent boundary layer.

Through greatly improved technology over the last century, the realm of high-speed flight has become the reality for many modes of transportation and weaponry. Aircraft, rockets, missiles, projectiles, and re-entry vehicles which will experience hypersonic flight conditions as a part of their intended operation have already been

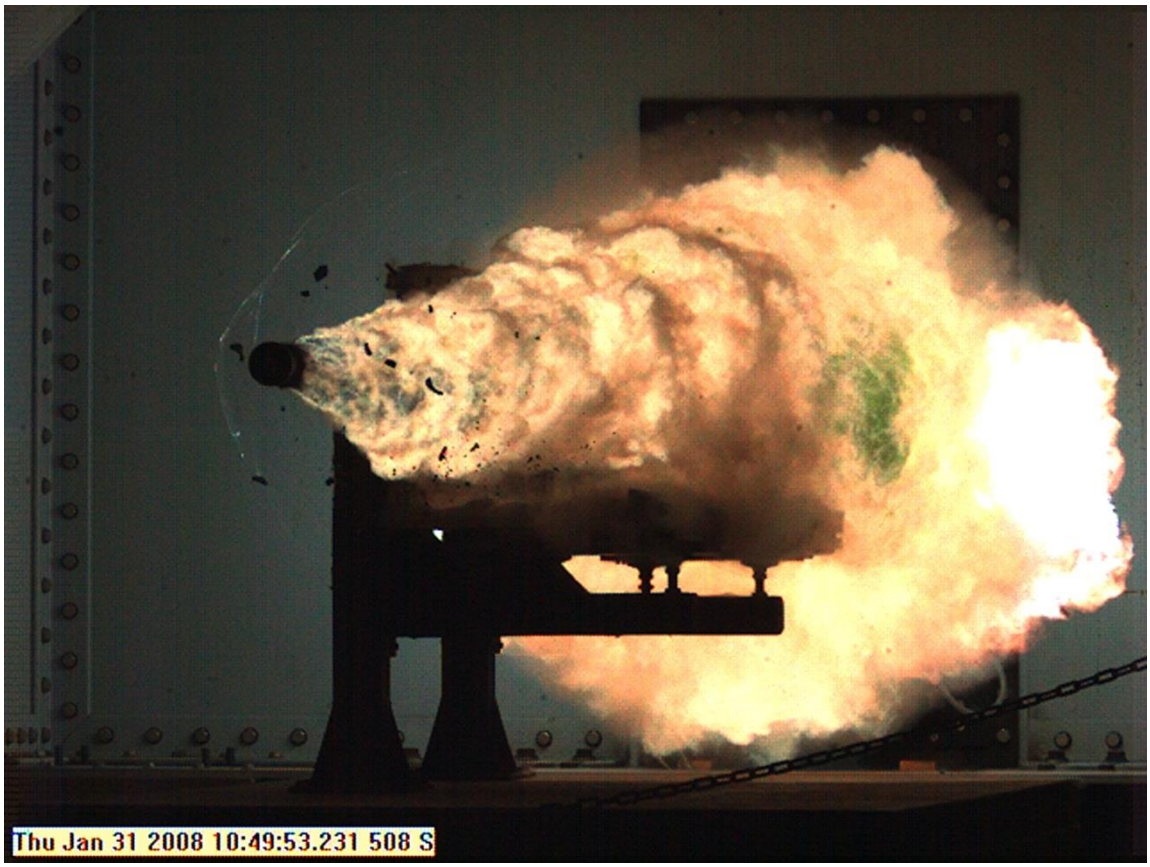

Fig. 2: Test firing of an EMRG at $M \approx 7.5$. Figure taken from Ref. [2].

designed or are currently in the process of design and development. At these speeds, drag and heat transfer become crucial design concerns. Figure 2 shows a test-firing of the electromagnet rail gun under development by the Office of Naval Research. In this image, the projectile is travelling at Mach number, $M \approx 7.5$. Notice the high levels of turbulence visible in the air immediately surrounding the projectile, as well as the obvious ionization of the air that is taking place. Skin friction drag and heat transfer will play a crucial role in the flight of this projectile, and other objects like it under similar flight conditions.

High velocities lead to high Reynolds numbers, which can cause the onset of turbulence to occur rapidly. With the increased momentum and heat transfer that accompany turbulence, it is vital for the survival and success of modern technology to understand the properties of turbulent structures present under such conditions.

Early work in the field of turbulence study identified the existence of large-scale structures through the use of simple flow visualization techniques such as smoke flow, die injection, and similar means. While this early work concentrated on low-speed turbulent flows, later techniques such as hot-wire anemometry revealed the presence of similar structures in high-speed flows. With the introduction of flow visualization techniques such as particle image velocimetry (PIV) as a means to study turbulent structures in the 1990s, it became possible for deeper studies into large-scale streamwise turbulent structures to take be made.

As early as 1972, Owen & Horstmann [3] identified the presence of large scale turbulent motions in a $M = 7$ boundary layer which were coherent enough to be convected multiple boundary layer thicknesses downstream. By the 1990s, low speed turbulent boundary layer structure was relatively well understood, including the presence and behavior of large-scale streamwise turbulence structures. Robinson [4] and Panton [5] both widely examined and summarized the existence of these structures in incompressible low-speed flows. Smith & Smits [6] conducted a study of a $M = 2.9$ airflow which indicated the presence of large scale turbulence motions similar to those described earlier in subsonic flow studies by Head & Bandyopadhyay [7]. However, when Smith et. al. used Rayleigh scattering to study a $M = 2.9$ flow from the spanwise-

streamwise orientation, they failed to identify the presence of large-scale streamwise elongated structures. Similarly, a second study by Smith, Smits & Miles [8] was unable to find evidence of large scale streamwise turbulent structures using Rayleigh scattering in a $M = 2.9$ flowfield. Further high speed studies by Ganapathisubramani, Longmire & Marusic [9] and Tomkins and Adrian [10] used PIV to identify the presence of long relatively high and low speed regions in the streamwise direction.

Given the conflicting information then present, Ganapathisubramani [11] conducted the first dedicated study of large scale streamwise turbulent structures in high speed flow using wide-field PIV in a $M = 2$ flowfield. This study concluded that strips of low and high speed fluid were present and coherent over large distances in the streamwise direction at boundary layer heights of $y/\delta = 0.2$ and 0.45. Figure 3 presents an example of these structures, showing examples of instantaneous vector fields of the streamwise velocity, u, normalized by the skin friction velocity, u_τ. In this image, red and blue represent relatively high and low speed structures respectively. Notice how the bands are clearly defined, and stretch over multiple lengths of δ in the streamwise direction. It was also found that the structures were compact in the spanwise direction, generally of a width equal to δ. Two-point correlations conducted during this study showed long-tailed behavior which further evidenced the existence of large scale streamwise structures. Humble et al. [12] have also conducted studies of turbulent structures over shock/boundary layer interactions using tomography which gave some insight into the large-scale turbulent structures of these flows. To date, these are typically the only dedicated experimental studies of large-scale streamwise-elongated

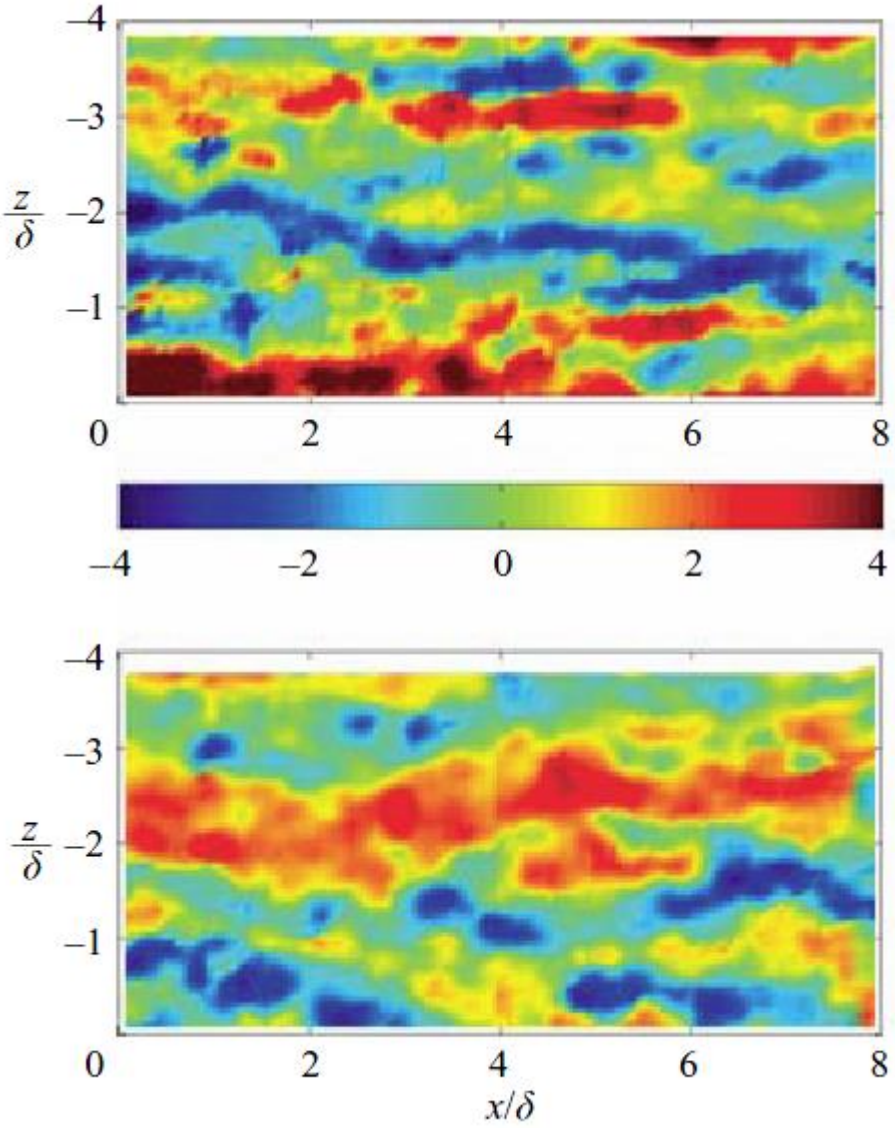

Fig. 3: Large-scale streamwise turbulence structures at $y/\delta = 0.16$ (top) and $y/\delta = 0.45$ (bottom) Figure taken from Ref. [11].

turbulence structures in compressible flow, although several other numerical studies exist [13].

The impact of varying pressure gradients on large-scale streamwise turbulent structures in high speed flow is even less explored. Numerous studies have been

conducted in low speed flows in order to determine the impact that differing pressure gradients have on boundary layer turbulence structures. Studies conducted by Bradshaw [14] were the first to examine the direct impact of curvature driven streamwise pressure gradients on turbulence properties. Spina, Smits, & Robinson [15] continued this line of study by showing the impact of both favorable and adverse pressure gradients on turbulence properties. These studies showed that adverse pressure gradients resulted in greater turbulence levels with destabilized flow, whereas favorable pressure gradients led to stabilization of the flow and decreased levels of turbulence. However, both of these studies dealt purely with airflow in the low speed or low supersonic regime. The work of Tichenor [16,17] and Peltier [18,19] were the first to expand the study of the impact of a favorable pressure gradient on turbulence structure into the high supersonic realm, with both studies conducted in a $M = 4.9$ flowfield. However, both of these studies were taken with an emphasis on the boundary layer profiles and smaller scale turbulence statistics. Neither study considered the presence of large scale turbulence structures or the impact of favorable pressure gradient on them. Recent flow visualization work by Humble et al. [20] has demonstrated the response of large-scale flow structures to favorable pressure gradients in the same experimental setup as the present study. However, quantitative information regarding the large-scale structural response is lacking, and the spanwise organization of these structures remains unclear.

C. Research Objectives and Contributions

The present study will explore the presence of large-scale (length $> 2\delta$) streamwise-elongated turbulent structures at three boundary layer heights, $y/\delta \approx 0.2, 0.5, \& \, 0.9$, within the hypersonic boundary layer ($M = 4.9$). The effects of pressure gradient and boundary layer height on the turbulent kinetic energy (TKE) and Reynolds shear stresses will also be quantified. Specifically, this study will compare the influence of increasing boundary layer height and increasing favorable pressure gradient on the size, distribution, and statistical correlation of streamwise low and high-speed regions through the use of both visual comparison and mathematical autocorrelation functions. Finally, this study will attempt to analyze the impact of the introduction of a diamond roughness element on the large-scale streamwise-elongated turbulence structure present in the high supersonic regime.

To our knowledge, this study will be the first dedicated exercise in experimentally identifying the presence of large-scale streamwise-elongated structures in a flowfield of $M > 2$. This is also the first study which attempts to quantify the impact of varying favorable pressure gradients and differing boundary layer height locations on the size, regularity, and distribution of these structures. Finally, this study is the first at these conditions to attempt to experimentally identify the impact of a roughness element on the properties of these large-scale structures. The results of this study should provide valuable in further characterizing the large scale motions present within the high-speed turbulent boundary layers, about which so much is still to be learned. This is considered

a key step in advancing our understanding of the turbulent boundary layer phenomenology present within high-speed flows, which will help provide the knowledge necessary for practical hypersonic vehicle and projectile design.

CHAPTER II

EXPERIMENTAL SETUP AND APPROACH

A. Facilities

The current study used a high-Mach number blow-down wind tunnel which is part of the National Aerothermochemistry Laboratory located at Texas A&M University. The tunnel was designed in an effort to study high supersonic and hypersonic air flows at moderate Reynolds numbers [19]. This tunnel is fed by a $23m^3$air tank capable of being charged to 2500 psi. The tunnel can operate until the tank pressure has been discharged to approximately 1300 psi, at which point the diffuser begins to stall, and the tunnel unstarts. A maximum 2500 psi charge provides a run time of approximately 30 minutes. Air is piped from the storage tank through a series of two inch stainless steel piping, as well as assorted pressure regulators and valves, through the heating elements and into the tunnel settling chamber. The facility piping is explained in great detail by Tichenor [16].

In order to prevent liquefaction of the air within the nozzle and test section, it must first be heated before entering the tunnel. This is accomplished through the use of a Chromalox 535 kW circulation heater model GCHI-108-535P-E4. Control settings for the heater are identical to those used by Peltier [19]. Due to the small size of this particular tunnel, the natural temperature oscillations within the heater control system would cause the tunnel to experience temperature swings outside of the desired range.

Therefore, the heating elements were manually activated by a switch on the tunnel control panel located next to the nozzle and test section.

Figure 4 shows a Solidworks model of the wind tunnel used in this experiment. In this figure, the settling chamber inlet is to the far left, followed by the nozzle, test section, diffuser, and finally the muffler on the far right. Air enters the tunnel through the settling chamber. From the settling chamber, the flow is forced into the nozzle. The nozzle is made of Type 347 Stainless Steel and has a throat height of $0.305cm$. The nozzle exit size is$7.62cm\ x\ 7.62cm$. After leaving the nozzle, the flow is blown through the test section where a series of windows on the sides and an acrylic ceiling allow horizontal laser entry as well as image collection from the top-down orientation. Testing done by Tilmann et al [21] during the tunnel design showed that this particular nozzle gives an output of $M = 4.89$. The exit boundary layer height is approximately $0.8cm$

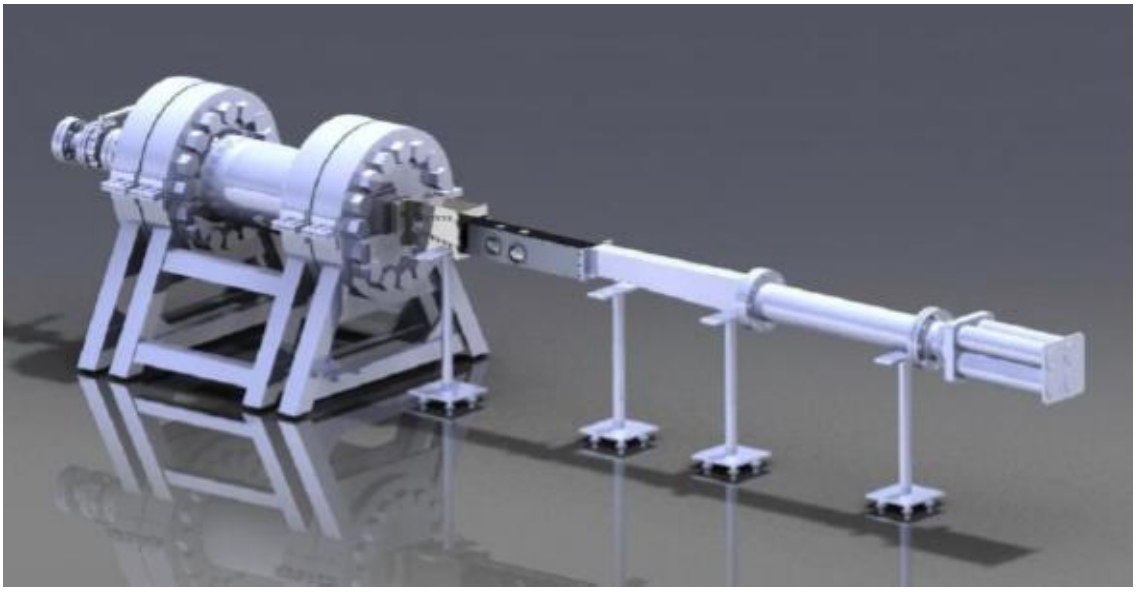

Fig. 4: Mach 5 blow-down tunnel configuration. Figure taken from Ref. [19].

and the flow is uniform over the center 80% of the flowfield [19].

Air leaving the nozzle exits into the test section, which has a constant cross section of $7.62cm\ x\ 7.62cm$ over its entire length of $71.12cm$. Both tunnel side walls are made out of aluminum, and include alignment dowel pins to precisely align the acrylic floor and ceiling sections during assembly. Both ends of the test section have bolts which allow transverse and rotational alignment to precisely match the nozzle exit. The nozzle end of both side walls of the tunnel include removable sealed access ports which allow for visual and tactile alignment of the tunnel floor, walls, and ceiling during assembly. Previous experiments run on this facility used an aluminum test section ceiling with a fused silica port to allow the laser sheet to enter into the test section vertically. For this particular study, a new tunnel ceiling was machined out of acrylic to allow for vertical optical access with an increased field of view. The acrylic ceiling was manufactured to the same dimensions as the previous aluminum ceiling described by Tichenor [16]. However, the bolt hole directly adjacent to the optical access point was omitted in order to allow for a wider field of view.

After exiting the test section, airflow passes through the diffuser where it is choked back to subsonic flow and exhausted through a muffler on the outside of the building and into the open atmosphere. The diffuser design includes an adjustable throat which allows for opening and closing the diffuser in order to maintain the proper throat height necessary to choke the varying pressure gradients tested.

Four test cases were considered in the present study, a flat zero pressure gradient model (ZPG), a slightly favorable weak pressure gradient model (WPG), a strong favorable pressure gradient model (SPG), and a flat zero pressure gradient model covered in diamond roughness elements (RZPG). These models were originally designed by Ekoto [22,23] and are the same ones used by Peltier [19,24] in his studies. The models are acrylic, and comprise the entire floor piece of the test section so that they are interchangeable. The ZPG model is a smooth, flat acrylic plate. The WPG and SPG models are described by the following polynomial: $Y = A(X - X_1)^3 + B(X - X_1)^2$. Table 1 shows the specific coefficients used for each model. Figure 5 shows a visual representation of the different floor model profiles and the global coordinate axis. Note that X and Y refer to the global coordinate system of the wind tunnel itself. The local wall coordinates x, y, and z will be used for the remainder of this document. X_1 and X_2 refer to the axial location where the curvature begins and ends respectively. The center of the test section window/viewing area is located at $X = 29.8cm$. At this location, the

Table 1: Pressure gradient model curvature coefficients. [19]

Model	A	B	X_1	X_2
WPG	6.423E-05	-3.757E-03	24.54	63.54
SPG	1.107E-05	-2.507E-03	24.54	39.64

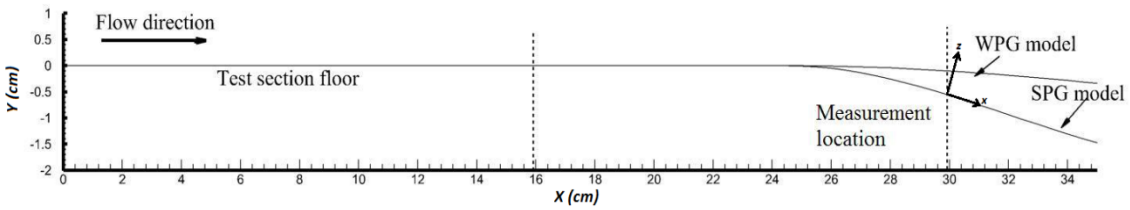

Fig. 5: WPG and SPG floor model profiles. Figure taken from Ref. [19].

local curvature of the wall is 1.7 degrees for the WPG model and 9.7 degrees for the SPG model.

The RPG model is a flat plate acrylic model with embossed diamond roughness elements covering the upper surface. The dimensions and distribution of the roughness elements are shown in Figure 6.

The coordinate system within the test section is arranged so that the *x*-axis is measured in the surface-tangential streamwise direction of the flow. The *z*-axis is measured in the spanwise direction, extending to the right with its origin at the left wall

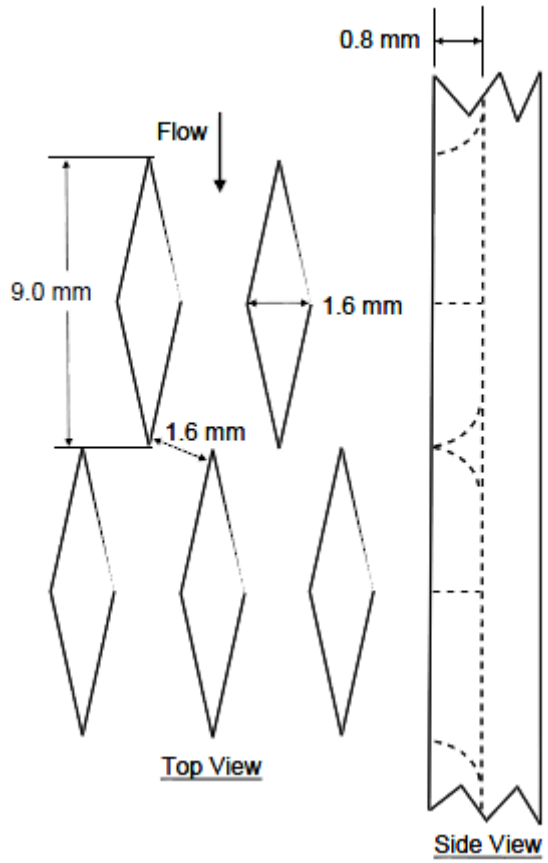

Fig. 6: Diamond roughness element topology. Figure taken from Ref. [22].

when viewed from the front of the test section. The *y*-axis extends upwards, perpendicular to the surface-tangential of the floor, with its origin at the top surface of the tunnel floor. See Figure 5 for further clarification.

The operating pressure and temperature of the tunnel were measured in both the settling chamber and the test section. The equipment used to measure these values is described in detail by Peltier [19,24]. The total temperature was measured using an Omega JQSS thermocouple and amplified using an OMNI AMP-IV amplifier. The total pressure was monitored via a pitot probe located in the settling chamber with an Endecvo Model 8540 $0 - 3048\,kPa$ high-temperature pressure transducer. An MKS Series 902 $0 - 101\,kPa$ pressure transducer was used to monitor the test section static pressure. The signal output from both pressure transducers and the thermocouple were collected by a National Instruments SC-2345 signal conditioner block followed by a National Instruments 6036E data acquisition board. Settling chamber pressure was set at $2400kPa$, controlled by a manual regulator, and settling chamber temperature was maintained at $360 \pm 5K$, as controlled by the manual on-off switch. This resulted in the test section conditions shown in Table 2.

Table 2: Test section tunnel operating conditions. [19]

Mach Number	Static Pressure (Pa)	Static Temperature (K)	Static Density (kg/m^3)	Re_θ
4.9	4800	63	0.27	~40,000

B. Particle Imaging Velocimetry

Particle image velocimetry is a nonintrusive technique to determine the whole-field instantaneous velocity of a flow. Although it requires extremely precise and accurate technology and equipment to conduct, PIV is a conceptually simple operation. In a PIV experiment, the airflow is first seeded with particles which are expected to track the flow accurately. These particles are then illuminated by a bright light or laser, formed and cut in a way so it only illuminates particles in a particular region or plane of interest. At the moment of illumination, an image is taken of the particles for reference. At a set length of time, Δt, later, the particles are illuminated again, and a second image is taken. The two pairs of images are then compared to track how each particle or group of particles moved from the first to the second image. By tracking the movement of each particle or group of particles, a vector field can be created for the entire image. Figure 7 shows a simple schematic of the PIV process in a wind tunnel using the side-view location.

In this particular setup, the flow was seeded with titanium dioxide (TiO_2) nano-particles. TiO_2 particles were chosen due to their high refraction and quick response time. Because the particles have a higher index of refraction, they scatter a significant amount of laser light. This allows a high level of contrast between the illuminated particles and the dark background. The small diameter of the particles allows them to respond quickly to changes in the flow, ensuring accurate fluid tracking of the particles. The manufacturer's quoted diameter of the particles is $200nm$. The particle response

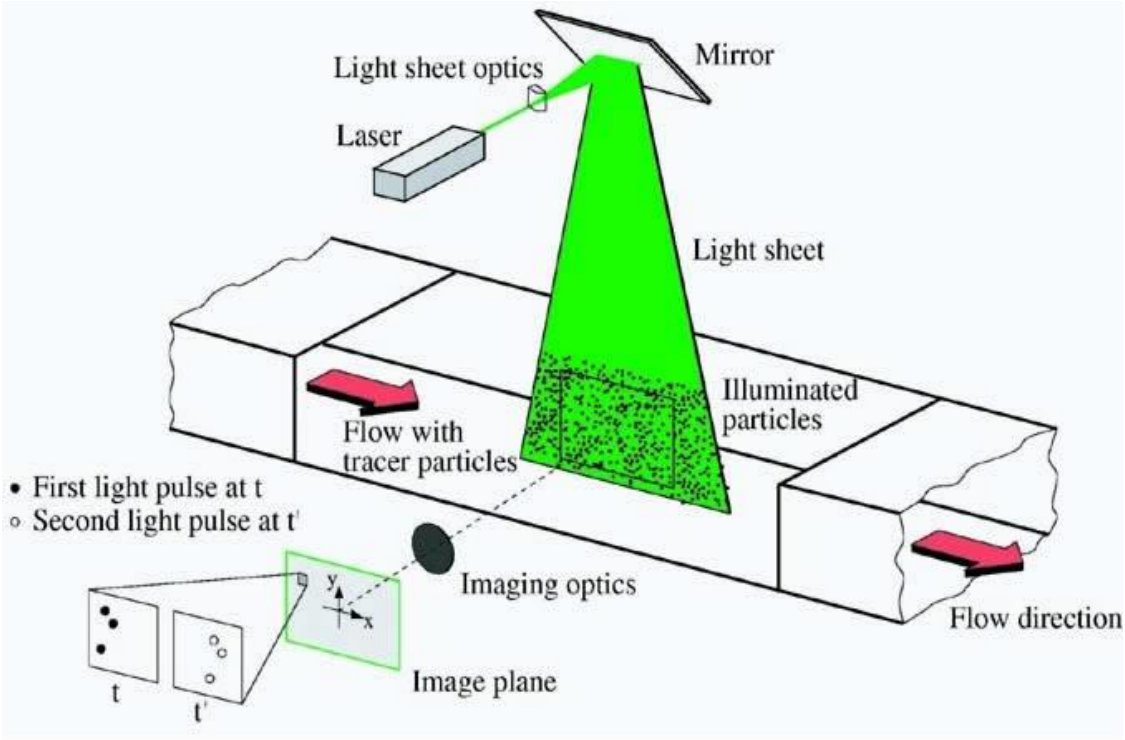

Fig. 7: Simple particle image velocimetry schematic. Figure taken from Ref. [25].

time was estimated at $\tau_p \approx 2.5\mu s$, based on Ragni et al.'s [26] comparative study. A flow time scale can be calculated using the baseline model as $\tau_f = \delta/U_\infty = 14.3\mu s$. The resulting Stokes number, $S_t = \tau_p/\tau_f \approx 0.17$, allows for the assumption that the particles are in fact reliably tracking the flow [19,24].

Injection of the TiO_2 particles was accomplished via a strut of $10mm$ in diameter mounted upstream of the wind tunnel nozzle. By using this injection location, a more even distribution of the particles into the boundary layer is expected. Seeding density was found to be sufficient at all boundary layer heights tested.

Figure 8-A shows an example image of the laser illuminated TiO_2 within the flow. Illumination of the particles was achieved using a dual-head New Wave Solo 120 Laser operating at a frequency of $10\,Hz$. The laser was operated at a wavelength of $532\,nm$ at an output of approximately $25\,mJ/pulse$. The laser beam was then directed through a $-25.4\,mm$ focal length cylindrical optic, which resulted in a laser sheet thickness of approximately $1\,mm$. Images of the particle refracted laser light were collected using a Cook PCO 1600 interline transfer CCD camera with a $1600x1200\,pixel$ resolution. The camera used a Nikon $f/4\ 60\ mm$ lens with an f-number of $f_{\#} = 8$. A circular polarizer was also used on the lens in order to minimize wall-reflected laser light while still ensuring adequate particle-reflected light collection. Timing of the laser and camera was set through a Quantum Composer model 9618 pulse generator, so that images were generated in matched pairs with a set time delay, $\Delta t = 500\,ns$, between them. Camware V2.19 software recorded the images from the camera. The PIV parameters used in this study were developed using the experiments made by Peltier [19,24], and were only slightly modified to meet the requirements of the different orientation used here.

Due to the top-down orientation of the current study, several modifications had to be made to the optical and laser mounting setup. An aluminum railing frame was set up above the tunnel in order to mount the camera above the test section in a vertical orientation. The laser was aligned in the spanwise direction through the side-wall fused silica windows. Figure 9 & 10 show the laser sheet and camera orientation relative to the wind tunnel.

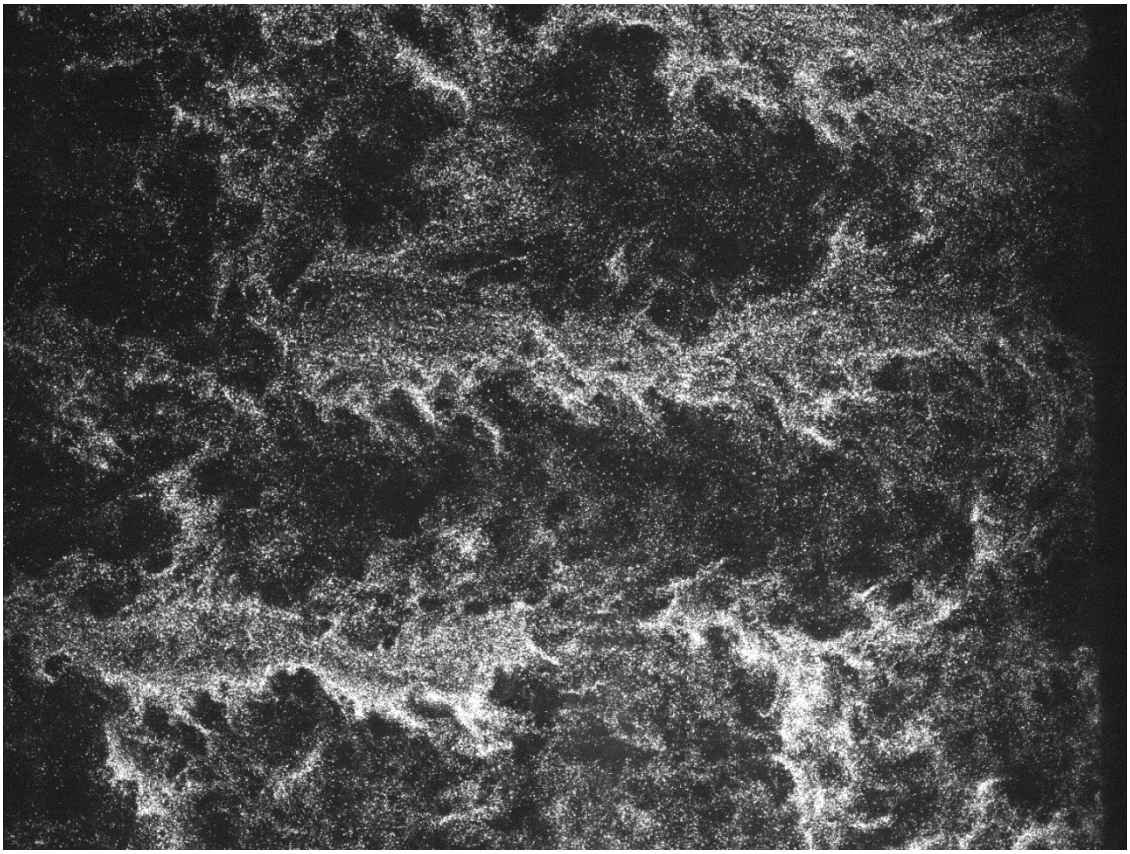

Fig. 8: Illuminated particles over the WPG model at the $y/\delta \approx 0.9$ location.

In order to analyze different boundary layer heights and pressure gradients, the laser sheet needed a provision for both vertical traversing motion and rotation about the *z*-axis. This was accomplished by mounting the beam directing mirrors on a vertically adjustable jack. By moving the jack up, the laser could remain stationary and still produce a horizontal sheet at any desired height within the jack's range of motion. Rotation around the *z*-axis was accomplished by mounting the cylindrical lens to an angle-adjustable pedestal. This allowed the laser sheet to be fully adjusted in the $x - y$

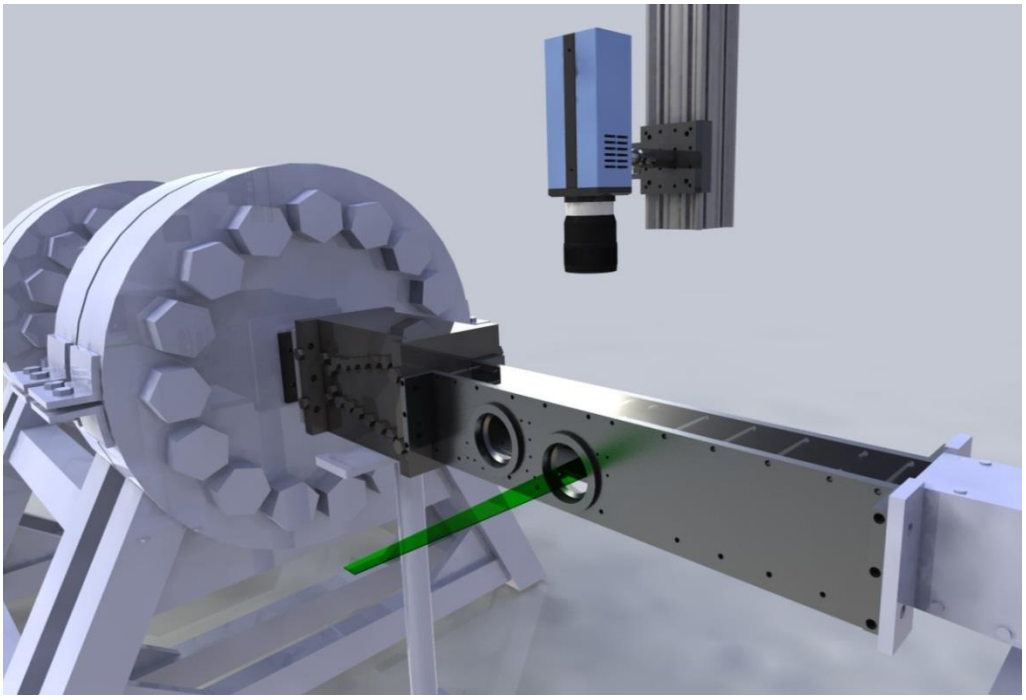

Fig. 9: Camera and laser alignment in the wind tunnel.

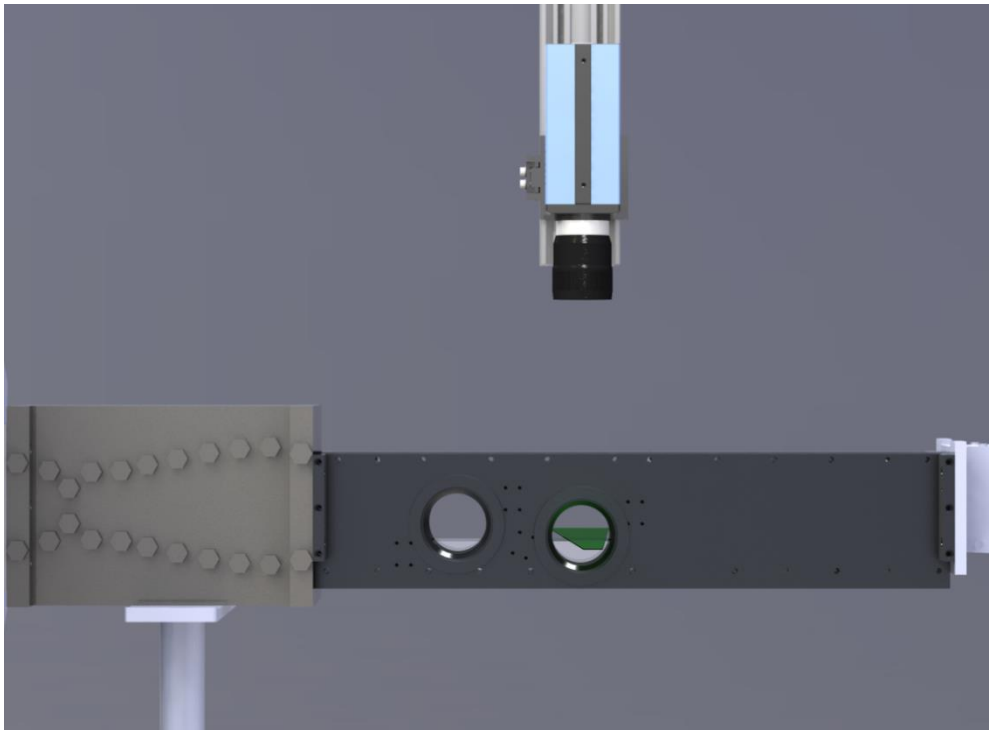

Fig. 10: Camera and laser sheet location for ZPG/WPG models.

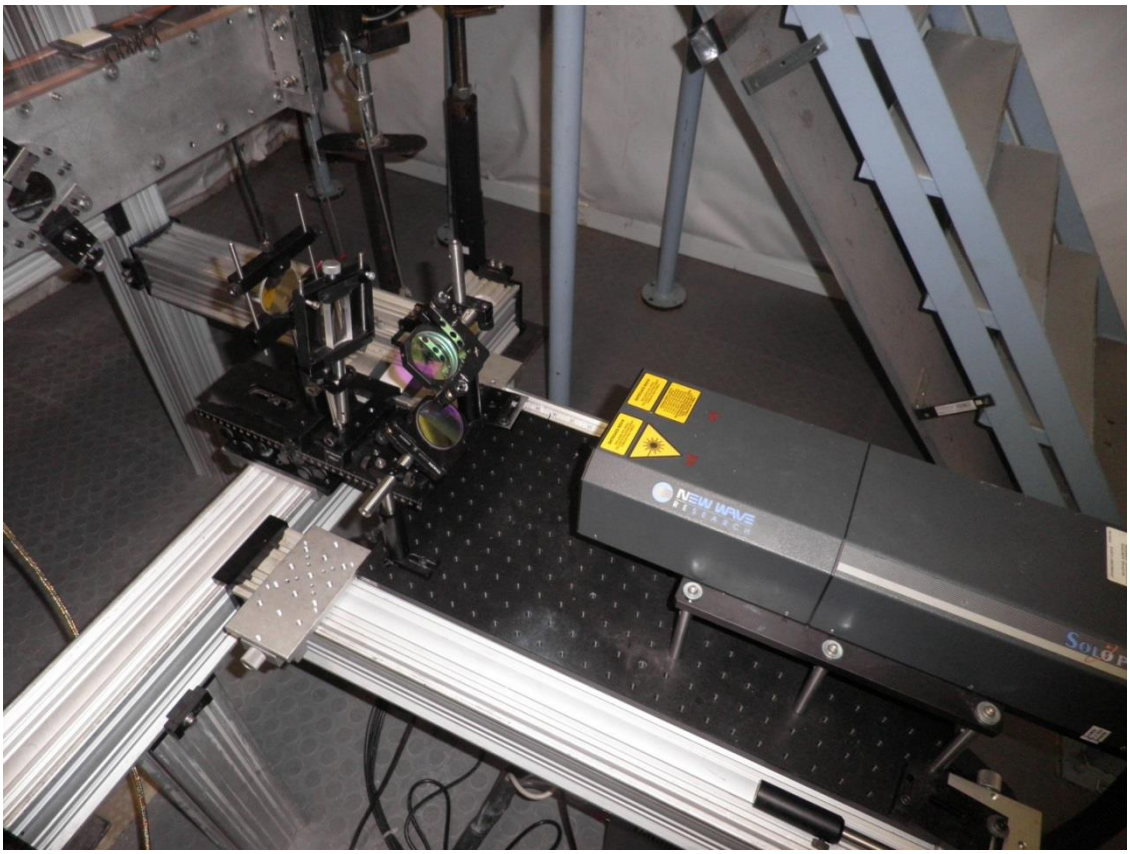

Fig. 11: Laser sheet alignment apparatus and knife edge filter.

plane in order to closely match the tangent of each floor plate curvature. Also, in order to clean up the vertical and horizontal edges and create a “top-hat” intensity profile of the laser sheet, an apparatus was designed which mounted two razor blades to thethe near-side wall silica window. This apparatus was also fully adjustable to match the floor profile and boundary layer height. Figure 11 shows an image of the beam directing and adjusting apparatus between the laser and the test section, as well as the razor-blade knife-edge filter. Note that the filter is fully open in this image for adjustment of the laser height.

Table 3: Laser sheet adjusting shim height.

Shim Heights (mm)				
Floor Model	$y/\delta \approx 0.2$	$y/\delta \approx 0.5$	$y/\delta \approx 0.8$	δ
ZPG	2.41	5.33	8.64	10.9
WPG	2.41	5.33	8.64	10.0
RZPG	2.41	5.33	8.64	11.3
SPG	4.78	6.99	11.20	12.9

In order to properly align the horizontal laser sheet at each boundary layer height, a series of nylon shims were manufactured. These shims were made in a rectangular shape with square cut ends that were the same $76.2\ mm$ across as the tunnel test section. The shim was inserted into the tunnel prior to each run, and the laser alignment and trimming apparatus was adjusted until the laser sheet cut just across the top x-z plane of the alignment shim. The ZPG, WPG, and RZPG models all used the same shims, since there was negligible difference between their respective δ. However, the SPG had a separate set of alignment shims, since its δ was significantly higher than the other three models. Table 3 includes the specific shim heights for each boundary layer height and profile.

Further modifications were made to the floor models of the test section in order to optimize the experiment for vertical optical alignment. In previous experiments by Ekoto [22,23], Tichenor [16,17], and Peltier [19,24], the acrylic floor sections were left transparent so that the laser sheet would exit through the bottom of the test section with minimal reflection. In this particular study, the laser entered and exited the tunnel horizontally through fused silica windows on both side walls. As such, light transmittance through the tunnel floor was no longer desirable. Since optical access was

now vertical, the floor needed to provide a high contrast image backdrop with as little external light transmittance as possible. Each acrylic floor model used in this study was thoroughly cleaned and painted flat black to minimize light transmittance and scattering reflections while maximizing contrast with the bright white particles.

Finally, in order to compensate for the increased angle compared to the other profiles tested, the camera mounting location and angle had to be modified while testing the SPG model. The camera was offset and angled to maintain the same distance and orientation between the tangent of the SPG curvature profile and the surface of the ZPG

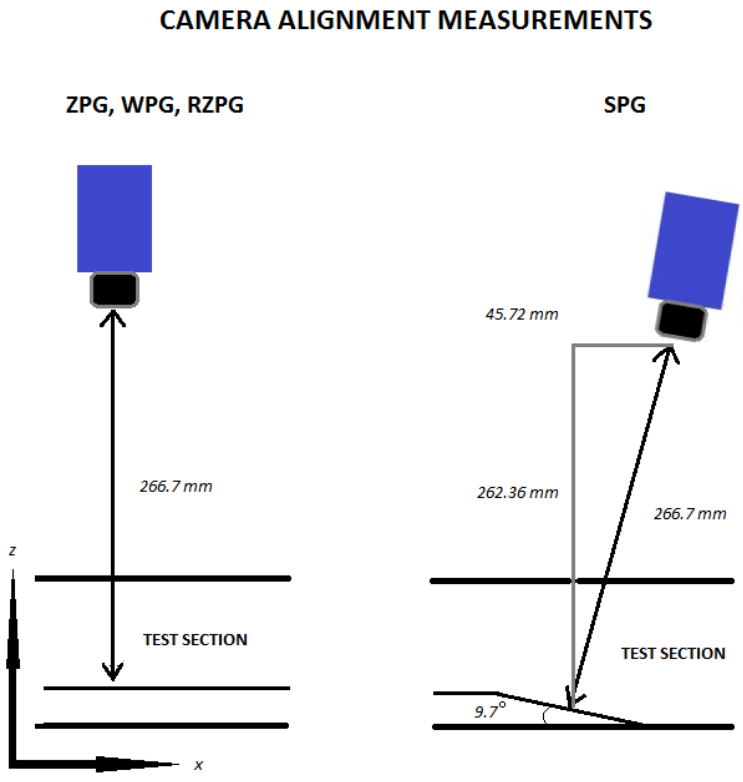

Fig. 12: Camera mounting location and orientation vs. floor model profile.

floor model. Figure 12 shows the method and measurements in which the camera was offset to maintain the same field of view and orientation between the different profiles.

C. Procedure

Four different floorplate models were tested, each at three different boundary layer height locations: $y/\delta \approx 0.2, 0.5, \& \, 0.9$. Each profile and boundary layer height was collected during one run-sequence of the wind tunnel. Wind tunnel operation was ceased between each boundary layer height and model profile in order to allow for adjustment of the laser sheet height and/or replacement of the floor section. Each run contained four image dumps of 345 image pairs each. This resulted in 1380 image pairs for each floor profile and boundary layer height location. Any run which experienced excessive TiO_2 residue streaking, seeding density problems, or notable misalignment of the field of view was repeated. The floorplate and acrylic ceiling was cleaned via the side-wall access ports between each run in order to help reduce particle residue and streaking. Wind tunnel equipment failure also resulted in several aborted runs. In total, 17 runs of the wind tunnel were completed, out of which, 12 useable sets of data were returned.

CHAPTER III

DATA ANALYSIS

A. Image Pre-Processing

The saved raw image pairs from each run were imported into XnView image processing software in order to prepare them for later vector field processing. Each raw image was rotated to compensate for a y-axis camera rotational misalignment of approximately $-2.6°$. This misalignment was noticed during review of the calibration and location images, as well as initial processing of the average spanwise velocity, W, for each image set. After rotating the image to compensate for this misalignment, each image was then cropped to remove the edges of the laser sheet and ensure the proper overall image size was evenly divisible by 32 pixels, as required by the image processing software. The images were then flipped horizontally to ensure a positive streamwise velocity, U, when the image processing was complete. A copy of each original image was created, along with notes on the exact operations taken on each image set. An example of one of the rotated, cropped, and flipped images from the ZPG model at $y/\delta \approx 0.9$ is shown in Figure 13. Once pre-processing was complete, the images were imported as image pairs into DaVis 8.0 intelligent image software by Lavision for determination of the vector fields via cross-correlation.

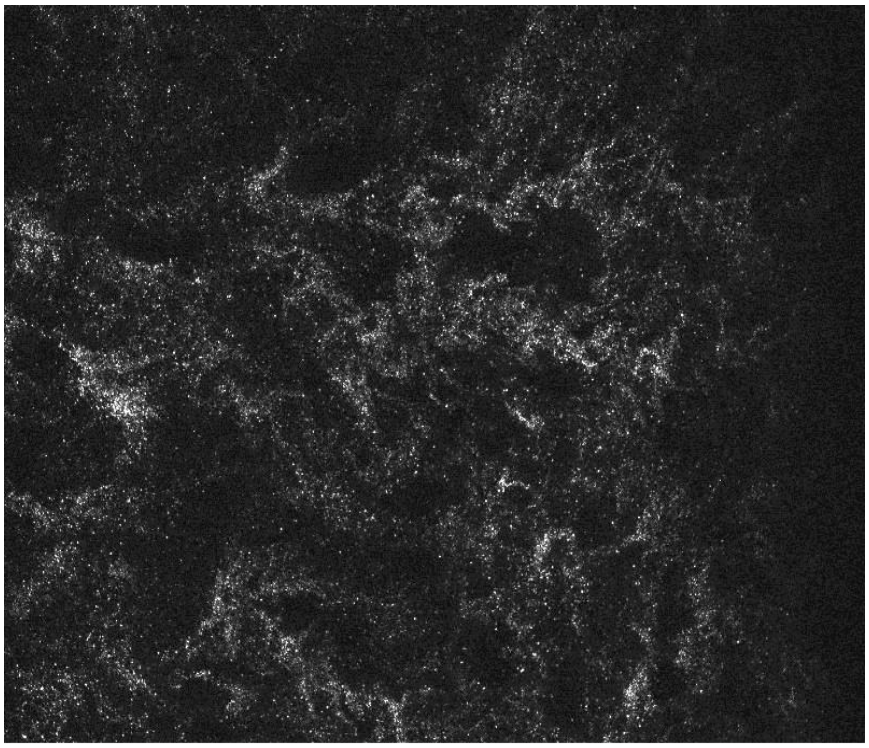

(before)

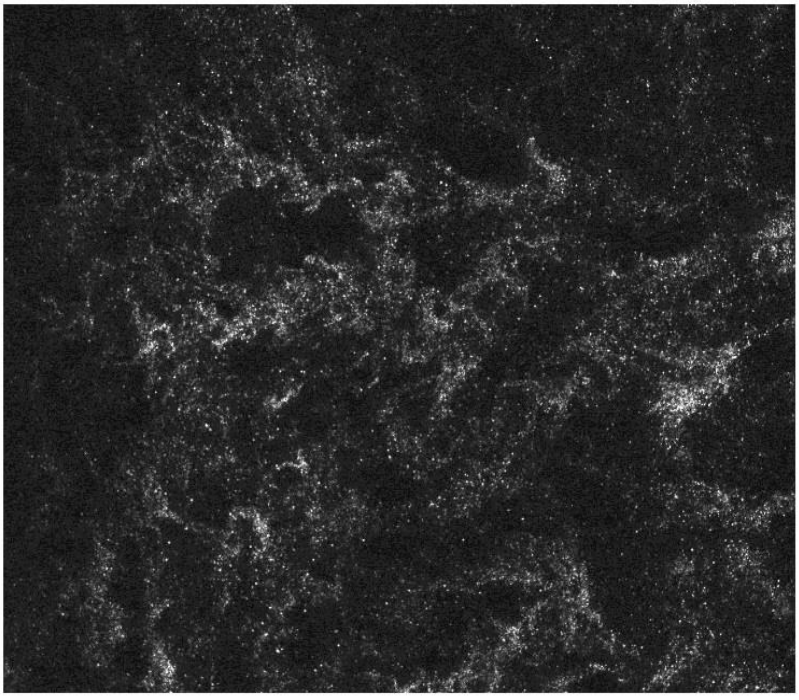

(after)

Fig. 13: Before and after example of pre-processed images.

The digital resolution of each test case was calculated using the calibration and location images saved for each data set. This information would particularly useful in converting the $pixles/frame$ DaVis outputs to m/s measurements which would be required for analysis. The calculated digital resolution for all test cases was between 37 and 39 $pixels/mm$.

B. Image Processing

The image sets was processed through DaVis in order to create an instantaneous vector field from each image pair. Image processing was completed using the PIV operation built into DaVis. Vector calculation parameters were set to multi-pass decreasing size, with progressive passes taken: four times at the 128 x 128 $pixel$ size and three times at the 32 x 32 $pixel$ size, with a 50% overlap on each pass. This resulted in an average vector spacing of approximately $0.85mm$. Due to the difficulties of seeding high Mach number flow, regions of insufficient seeding were inevitable. In order to remove the erroneous vectors created by seeding deficiencies, a 2x median filter was employed to remove and replace bad vector locations via linear interpolation. After the empty spaces were filled, each vector field received a 3x3 Gaussian smoothing pass to complete image processing. The majority of these settings were used by Peltier [19,24], and only slightly modified for the present study. All vector fields were saved and exported as both Tecplot .dat files and ASCII .txt backup files for post-processing. Each vector field set was also ensemble averaged in DaVis to return the average values for streamwise velocity, U, spanwise velocity, W, the root mean square of the

streamwise and spanwise velocity fluctuations, u'_{RMS} & w'_{RMS}, the turbulent kinetic energy, TKE, and the uu, uw, and ww components of the Reynolds shear stress for each image set.

C. Image Post-Processing and Averaging

The bulk of image post-processing and averaging was completed using MATLAB code created specifically for this study. Each set of DaVis averaged data was combined into one TecPlot .dat file using MATLAB code originally written by Peltier [19,24] and modified for this experiment. Another program was then written to average the DaVis ensemble averaged output from the four image sets at each location. This code also calculated a single average streamwise and spanwise velocity for each test location. In some instantaneous images, drastic artificial velocity vectors were present due to effects imposed at the edge of the image or streaking/smudging within the field of view. By excluding values beyond 3σ from the initial average velocity, these artificial vectors were prevented from impacting the true average velocity of the image sets. Table 4 shows the 3-sigma averaged streamwise and spanwise velocities, $U_{3\sigma}$ & $W_{3\sigma}$, for each

Table 4: 3-sigma average U & W values for each location.

3σ Average Values (m/s)						
	$y/\delta \approx 0.2$		$y/\delta \approx 0.5$		$y/\delta \approx 0.9$	
Floor Model	$U_{3\sigma}$	$W_{3\sigma}$	$U_{3\sigma}$	$W_{3\sigma}$	$U_{3\sigma}$	$W_{3\sigma}$
ZPG	629.80	0.53	699.75	1.47	753.42	3.43
WPG	614.19	-0.55	686.94	0.51	738.47	0.06
RZPG	500.33	1.40	667.42	2.75	743.71	2.68
SPG	634.12	3.08	697.92	2.58	750.09	3.55

Table 5: Calculated boundary layer height for each location. [19]

Boundary Layer Height Location			
Floor Model	$y/\delta \approx 0.2$	$y/\delta \approx 0.5$	$y/\delta \approx 0.9$
ZPG	0.25	0.54	0.98
WPG	0.17	0.44	0.79
RZPG	0.17	0.48	0.85
SPG	0.19	0.48	1.04

test location.

The $U_{3\sigma}$ values for each location were then compared to data on the boundary layer profiles collected by Peltier [19,24], which allowed the approximate y/δ positions to be determined. Table 5 includes the calculated y/δ position for each data set collected.

The final step of this iteration of code was to create non-dimensionalized values to be exported into TecPlot. Using the previously determined digital resolutions, δ and $U_{3\sigma}$ values, the .dat files were configured with information for an x/δ and z/δ axis, as well as values of the streamwise and spanwise velocity of each *x,z* location in the field of view, U_{xz} & W_{xz}, in units of m/s. A final column was inserted containing the non-dimensionalized $U_{xz}/U_{3\sigma}$ for each data set.

The non-dimensionalized average velocity fields for each test location were also inspected to determine their range from the average $U_{3\sigma}$ value for each case. The distance from the mean value quantified the amount of laser sheet rotational misalignment about the x and z-axis in each run. The percentage spread of $U_{xz}/U_{3\sigma}$ was compared to the boundary layer velocity profile from Peltier's data [19,24] in order to

Table 6: Calculated boundary layer height misalignment for each location. [19]

Boundary Layer Height Span (%δ)			
Floor Model	$y/\delta \approx 0.2$	$y/\delta \approx 0.5$	$y/\delta \approx 0.9$
ZPG	±3%	±5%	±11%
WPG	±4%	±4%	±6%
RZPG	±4%	±8%	±10%
SPG	±3%	±4%	±12%

quantify the amount of misalignment in percentage of δ. These values can be found in Table 6.

Note that the $y/\delta \approx 0.9$ locations for the ZPG and SPG both have a considerable amount of spread. This is mainly due to the fact that $\frac{\partial U}{\partial y}$ is so small at such high locations in the boundary layer. It should be noted that the bulk of the image data is still well less than these percentage points, but underlying edge-effects and laser sheet thickness ($t_{laser} \approx 1\ mm$) tend to produce a higher level of uncertainty at higher y/δ levels due to the much smaller velocity gradient in the vertical direction. No significant axial rotation alignment issues were visually observed at these two upper locations using the averaged velocity images.

After the average values, resolutions, and boundary layer heights had been calculated, a separate code was created to non-dimensionalize the instantaneous image files. This allowed for visual comparison of the images during the final analysis process. The instantaneous images were also saved into Windows Movie file format, colored in set percentage variations from the average values. The percentage bands chosen were $U_{3\sigma} \pm 20\%$, $U_{3\sigma} \pm 12\%$, and $U_{3\sigma} \pm 5\%$ for $y/\delta \approx 0.2, 0.5, and\ 0.9$ respectively. These

values were selected to give the best contrast between the high and low speed regions present within each image set. When played in succession, these videos assist in recognizing the visual differences resulting from the unique behavior of the turbulent structure patterns at each test location.

D. Auto-Correlations

The final coding segment written in MATLAB was used to create autocorrelation profiles for each of the test conditions. These profiles are used to determine the statistical distribution of the structure sizes present within the image sets captured. By comparing the shape and size of these profiles, inferences about the general length, width, and recurrence of the large scale turbulence structures can be made.

In order to generate an autocorrelation profile, the average values for U_{xz}, W_{xz}, u'_{RMS}, and w'_{RMS} were calculated for each x-z location within the individual image sets. A series of loops were then written to traverse the image in both the x and z-axis directions, and calculate a correlation profile based on distance from the selected start point. The transverse correlations (z-direction) were calculated at each $\frac{1}{3}$ point along the central x-axis of the image. Likewise, the axial correlations (x-direction) were calculated at each $\frac{1}{3}$ point along the left edge and central z-axis of the image. The $\frac{1}{3}$ points were chosen because they allowed three times the number of correlation points to be calculated while still remaining statistically independent of each other, because they lay

outside the $\pm 1\,\delta$ statistically correlated structure distance that was observed to be prevalent throughout all test section locations in the transverse direction.

The axial correlations were taken from the left edge of the image in order to extend the correlation profile to the maximum distance possible. However, the high percentage of false vectors at the sides of the image prevented the correlations from starting at the extreme edge. In order to remove the impact of these artificial vectors, the axial correlation start points were moved incrementally in the positive x-direction until the first half of the correlation profile matched the axial correlation profiles taken from the central z-axis. This slightly reduced the field of view, but ensured accuracy for each profile. The autocorrelation equations for each velocity and direction are given by equations 3.1-3.4.

$$R_{ux} = \frac{u'(x) * u'(x+\Delta x)}{u'_{RMS}(x) * u'_{RMS}(x+\Delta x)} \tag{3.1}$$

$$R_{uz} = \frac{u'(z) * u'(z+\Delta z)}{u'_{RMS}(z) * u'_{RMS}(z+\Delta z)} \tag{3.2}$$

$$R_{wx} = \frac{w'(x) * w'(x+\Delta x)}{w'_{RMS}(x) * w'_{RMS}(x+\Delta x)} \tag{3.3}$$

$$R_{wz} = \frac{w'(z) * w'(z+\Delta z)}{w'_{RMS}(z) * w'_{RMS}(z+\Delta z)} \tag{3.4}$$

The correlation profiles were calculated for each image set. The four image sets at each test location were then averaged to give an overall correlation profile. The

distribution from each image set shared the same trends, and the averaging was done only to improve the statistical convergence of the final profile. The final correlation profiles for each location were then transferred to a separate MATLAB code, which generated the necessary plots to effectively compare the correlation profiles at each location.

E. Experimental Uncertainty

A 95% confidence interval was used to calculate the statistical uncertainty using the method outlined by Benedict & Gould [27], assuming a normal distribution of the instantaneous velocity fields over all 1380 realizations, N, for each test location. Equation 3.5 was used to calculate the percent uncertainties for each variable, ε_{var}, using the respective η values for each variable as shown in Table 7. The Reynolds shear stress correlation coefficient, ω, was determined using equation 3.6. $\omega = \frac{\overline{u'w'}}{(\overline{u'u'})^{1/2}(\overline{w'w'})^{1/2}}$. The uncertainties determined for $U_{3\sigma}$, $\overline{u'u'}$, $\overline{u'w'}$, & $\overline{w'w'}$ for each test condition are shown in Table 8. It should be noted that the percentage error for $\overline{u'w'}$ was determined as $\% \pm u'w'_{RMS}$, instead of percent $\% \pm \overline{u'w'}$.

$$\% \pm \varepsilon_{var} = \frac{1.96\sqrt{\eta/N}}{\varepsilon_{var}} \tag{3.5}$$

$$\omega = \frac{\overline{u'w'}}{(\overline{u'u'})^{1/2}(\overline{w'w'})^{1/2}} \tag{3.6}$$

Table 7: η-values for each variable. [27]

Variable	η-value
$U_{3\sigma}$	$\overline{u'^2}$
$\overline{u'u'}$	$\left(\overline{u'^2}\right)^2$
$\overline{w'w'}$	$\left(\overline{w'^2}\right)^2$
$\overline{u'w'}$	$(1+\omega^2)\left(\overline{u'^2}\right)\left(\overline{w'^2}\right)$

Table 8: Calculated statistical uncertainty for each test location. [27]

Statistical Uncertainty based on a 95% Confidence Interval				
Floor Model	Variable	$y/\delta \approx 0.2$	$y/\delta \approx 0.5$	$y/\delta \approx 0.9$
ZPG	$U_{3\sigma}$	0.41%	0.27%	0.12%
	$\overline{u'w'}$	2.91%	1.56%	2.55%
WPG	$U_{3\sigma}$	0.50%	0.25%	0.14%
	$\overline{u'w'}$	0.94%	5.03%	3.67%
SPG	$U_{3\sigma}$	0.24%	0.21%	0.14%
	$\overline{u'w'}$	0.45%	1.54%	1.28%
RZPG	$U_{3\sigma}$	0.64%	0.27%	0.13%
	$\overline{u'w'}$	4.51%	4.78%	3.52%
All Test Cases	$\overline{u'u'}$ & $\overline{w'w'}$	5.28%	5.28%	5.28%

CHAPTER IV

RESULTS AND DISCUSSION

A. Velocities, Reynolds Shear Stresses, and TKE

Averaged Data from each test condition in the favorable pressure gradient comparison is plotted in Figures 14 & 15. These plots include the values for $U_{3\sigma}$, ${u'}_{RMS}$, ${w'}_{RMS}$, TKE, and the uu, uw, & ww components of the Reynolds shear stress, $\overline{u'u'}$, $\overline{u'w'}$, & $\overline{w'w'}$ respectively, for each test model. The velocity profile is in excellent agreement with Peltier under these conditions, with the SPG showing a considerably higher $U_{3\sigma}$ than the ZPG or WPG test conditions in the near wall location. This is a result of the higher $\frac{\partial U}{\partial y}$ near the wall for the SPG test condition, and is the same behavior observed by Peltier in his earlier experiments [19]. Also notable is the fact that the TKE and Reynolds shear stresses decrease drastically for the ZPG and WPG models at the upper locations of the boundary layer, while they remain fairly constant throughout the boundary layer height in the SPG model. This is the same trend observed in the size and strength of the streamwise-elongated turbulence structures, as will be elaborated on later in this chapter. The ${u'}_{RMS}$ and ${w'}_{RMS}$ values also follow this trend, but to a lesser extent.

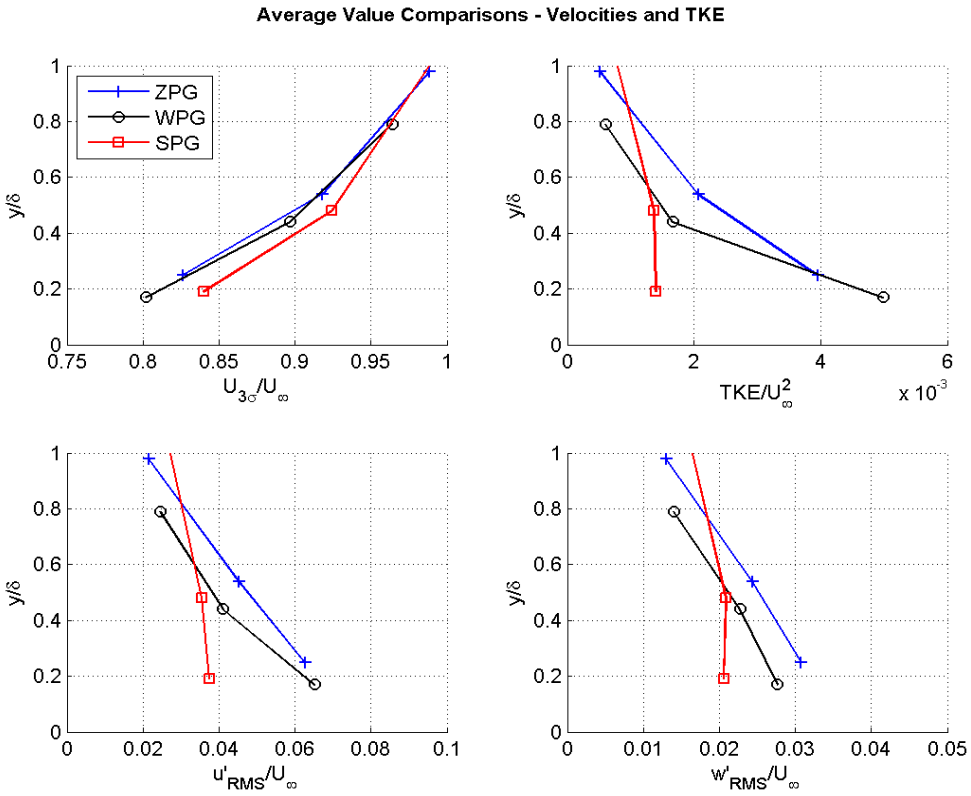

Fig. 14: Average velocity and TKE comparison.

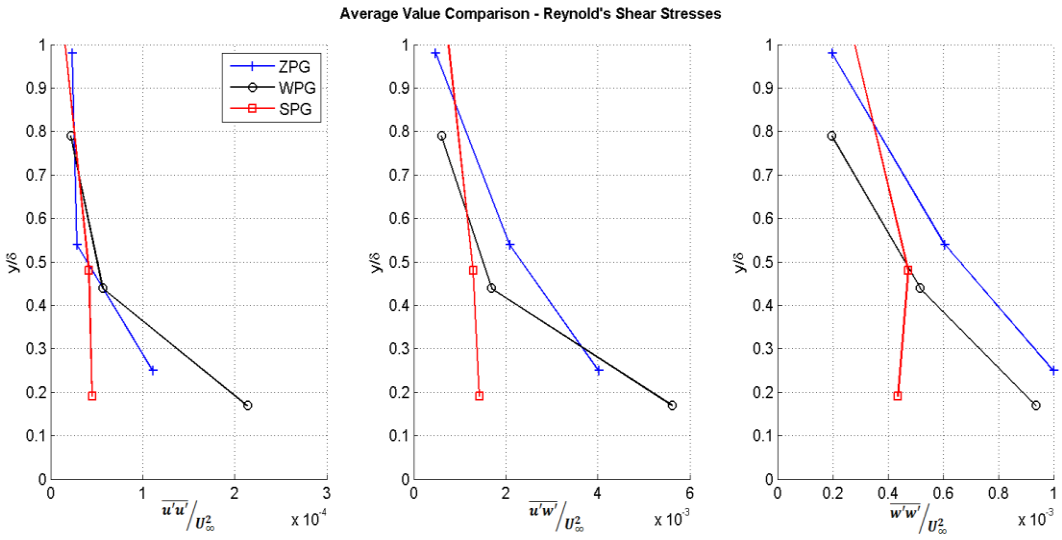

Fig. 15: Reynolds shear stress comparison.

B. Large Scale Turbulence Structure Identification

Large scale streamwise-elongated structures are visually present in every test condition. Figures 16-18 show instantaneous velocity fields selected for each floor section at $y/\delta \approx 0.2, 0.5,$ & 0.9 respectively. These images were hand selected from the data set in order to show some of the more pronounced appearances of the streamwise elongated turbulence behavior. Note that the image and color scaling is not the same for

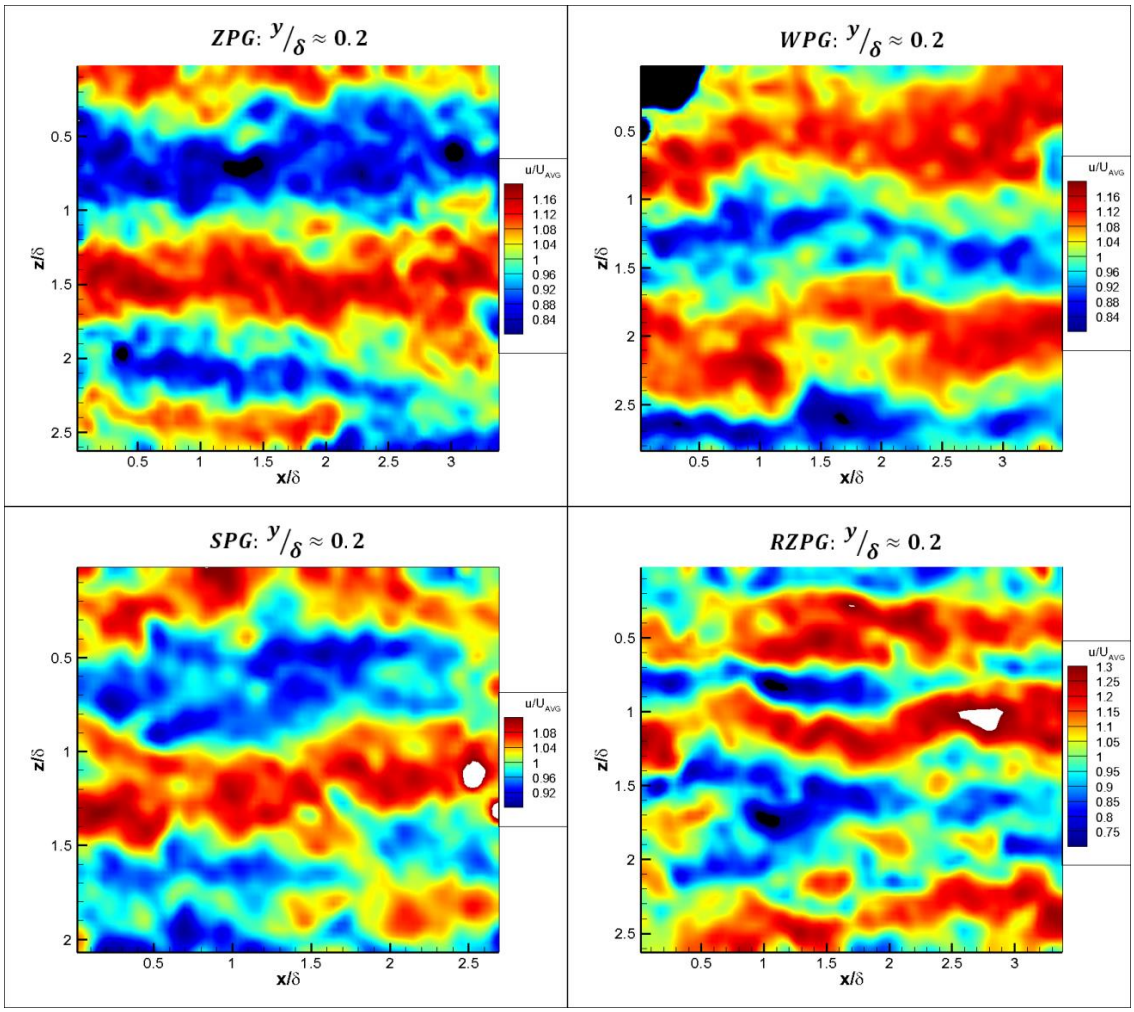

Fig. 16: Streamwise-elongated turbulence behavior at $y/\delta \approx 0.2$.

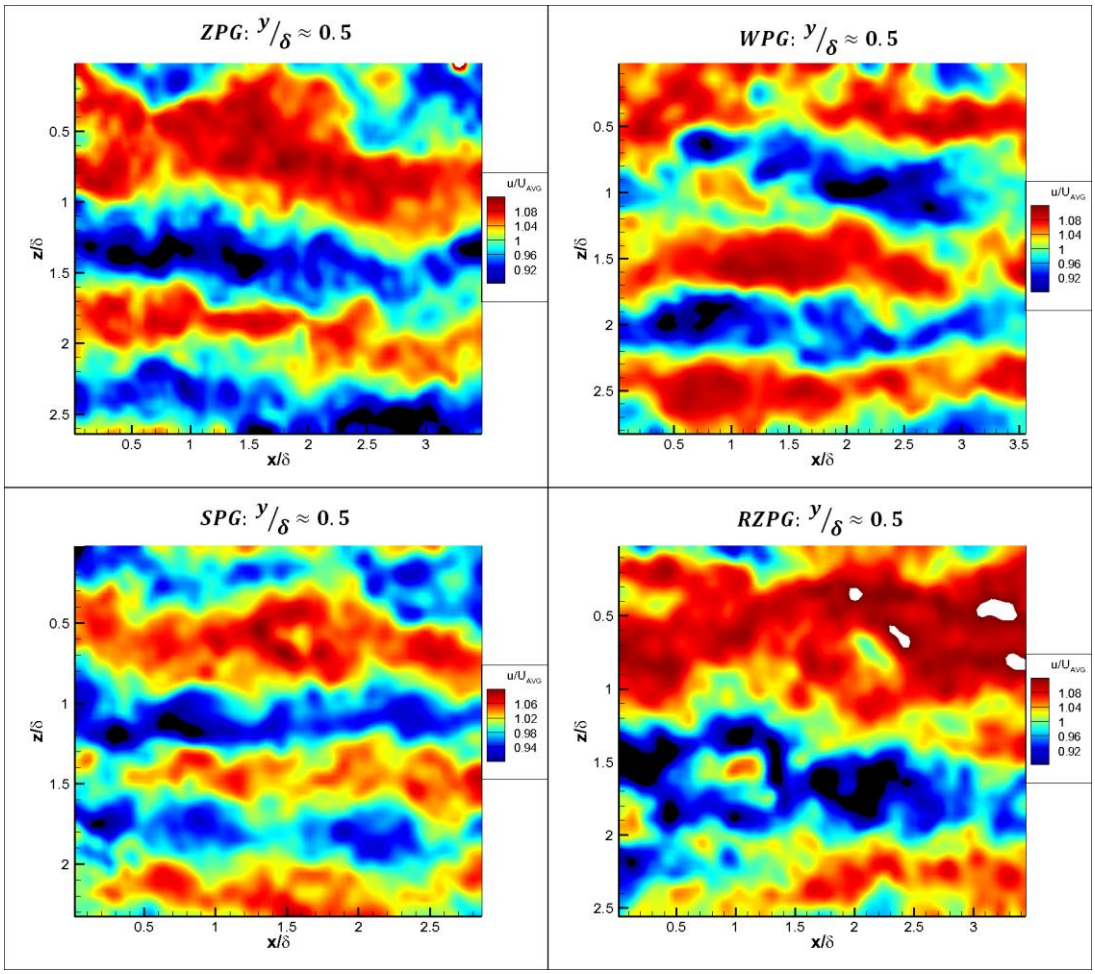

Fig. 17: Streamwise-elongated turbulence behavior at $y/\delta \approx 0.5$.

each velocity field. The velocity field color range was specifically selected to highlight the turbulence structure behavior for each case, and each image is scaled by $U_{xz} \pm$ a specific percentage of $U_{3\sigma}$. In regions of each image which are colored solid black, U_{xz} falls below the lower percentage limit of $\frac{U_{xz}}{U_{3\sigma}}$. Solid white indicates regions where U_{xz} is

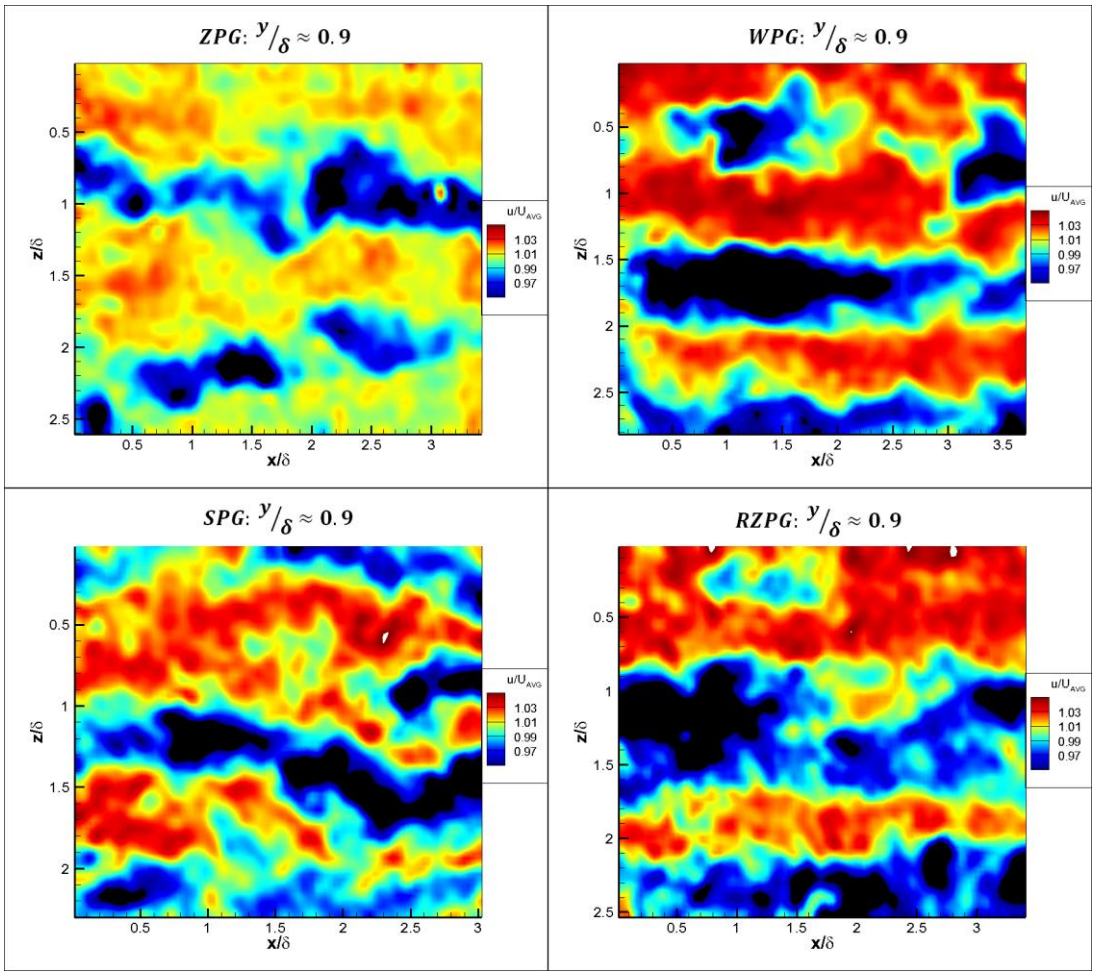

Fig. 18: Streamwise-elongated turbulence behavior at $y/\delta \approx 0.9$.

above the upper percentage limit of $\frac{U_{xz}}{U_{3\sigma}}$. In each of these figures, regions which are yellow, orange, or red have a value of U_{xz} which is increasingly higher than $U_{3\sigma}$: representing relatively high speed turbulence structures. Regions which are light blue or dark blue represent where U_{xz} is increasingly lower than $U_{3\sigma}$, denoting a low-speed turbulence structure. Notice that each test condition has one or more horizontal "bands" of alternating high and low speed flow regions. Some test conditions such as the ZPG at $y/\delta \approx 0.2$ have noticeably better defined structure, while most of the $y/\delta \approx 0.9$ cases

have very poorly defined structure. However, even in the uppermost boundary layer conditions, low speed streamwise-elongated structures are still present with a length $\geq 2\delta$.

C. Favorable Pressure Gradient Effects

Visual analysis of the instantaneous vector fields reveals a very clear distinction between the ZPG/WPG and SPG streamwise-elongated structures found at the $y/\delta \approx 0.2$ and 0.9 locations. There is a smaller yet still discernible difference between the SPG and the other two smooth cases at the $y/\delta \approx 0.5$ locations. While these differences are most visible in the video series of instantaneous velocity fields, they are also apparent in randomly selected velocity fields from each image set. Figures 19-21 show instantaneous velocity fields for the ZPG, WPG, and SPG models at each boundary layer height location tested. The four velocity fields per model in each figure are arranged vertically, and were chosen using a random number generator from each of the data sets. The images for each boundary layer location are scaled using the same percentage spread of the $\frac{U_{xz}}{U_{3\sigma}}$ values. Scaling values for these figures are $U_{xz} \pm 20\%\, U_{3\sigma}$, $U_{xz} \pm 12\%\, U_{3\sigma}$, and $U_{xz} \pm 5\%\, U_{3\sigma}$ at the $y/\delta \approx 0.2$, 0.5, & 0.9 locations respectively. The

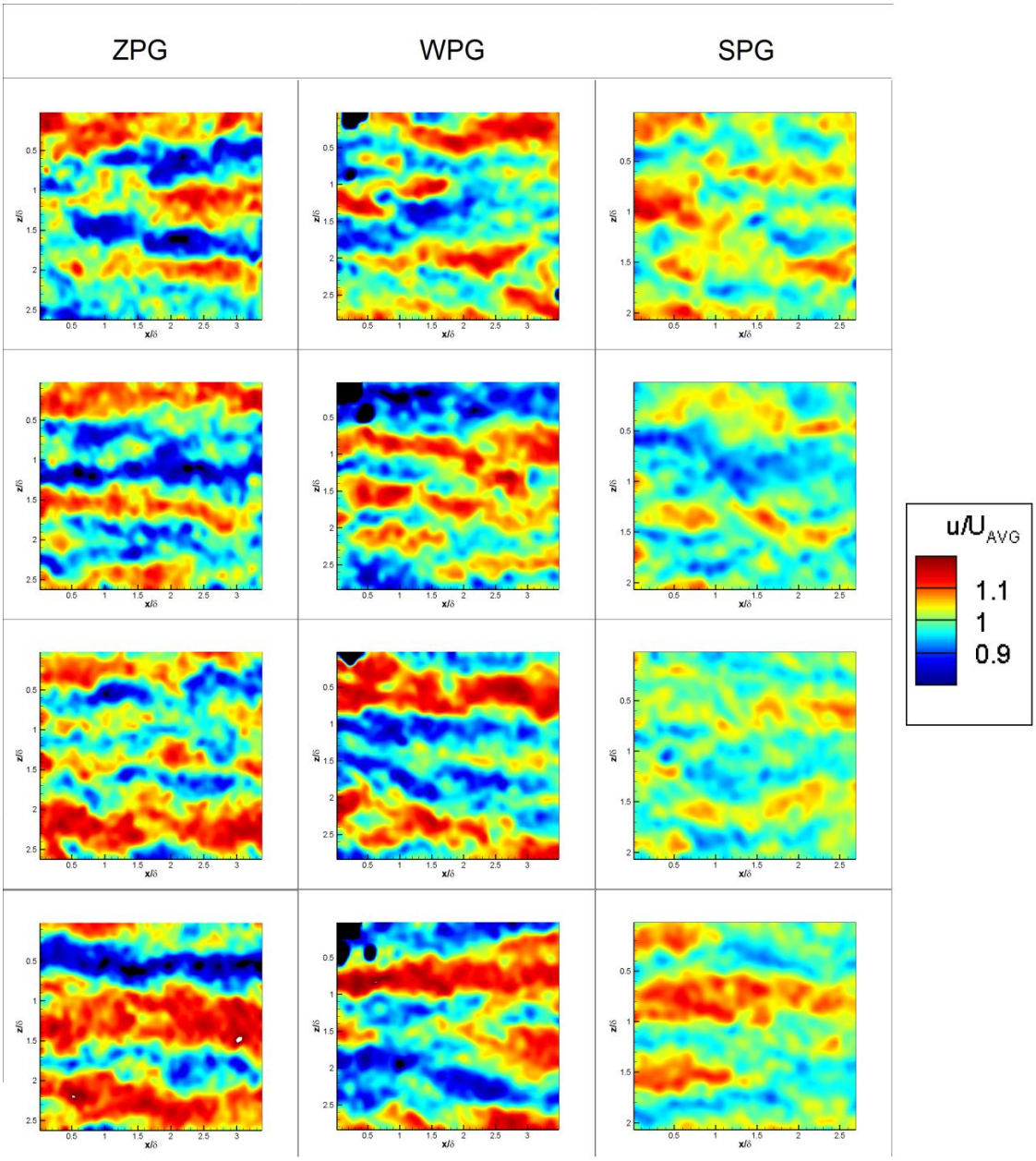

Fig. 19: Instantaneous velocity field comparsion at $y/\delta \approx 0.2$.

coloring spectrum for each of these data sets is exactly the same as was described earlier for Figures 16-18.

Looking at Figure 19, it is readily apparent that the ZPG and WPG models generate stronger and more organized streamwise-elongated turbulence structures. The

SPG velocity bands are much less intense relative to the average velocity, and they are more broken and scattered in the streamwise direction than the WPG or ZPG velocity bands. The more regular spanwise organization of the high and low speed structures in the ZPG/WPG models is also visually apparent. Combined, this represents a lack of streamwise and spanwise coherence in the SPG model relative to the other two. However, this trend does not hold at the $y/\delta \approx 0.5$ location, as shown in Figure 20. Notice at this location that the magnitude of the intensity of high and low speed regions compared to the average is approximately equal across the ZPG, WPG, and SPG conditions. It is difficult to comment on the relative spanwise or streamwise coherence of these structures, as there is little visual distinction between the three cases. When viewing Figure 21, it appears that the order of intensity is reversed compared to the lower boundary layer height. At $y/\delta \approx 0.9$, the SPG structures appear to have a greater magnitude disparity compared to the mean velocity, where the structures in the ZPG velocity fields are much less intense. The WPG structures are somewhere in between, but trend more towards the SPG case than the ZPG. It is visually apparent that the SPG and WPG velocity bands have more regular spanwise organization and distribution than the ZPG test case, but the difference in streamwise length of the three models is once again not readily apparent.

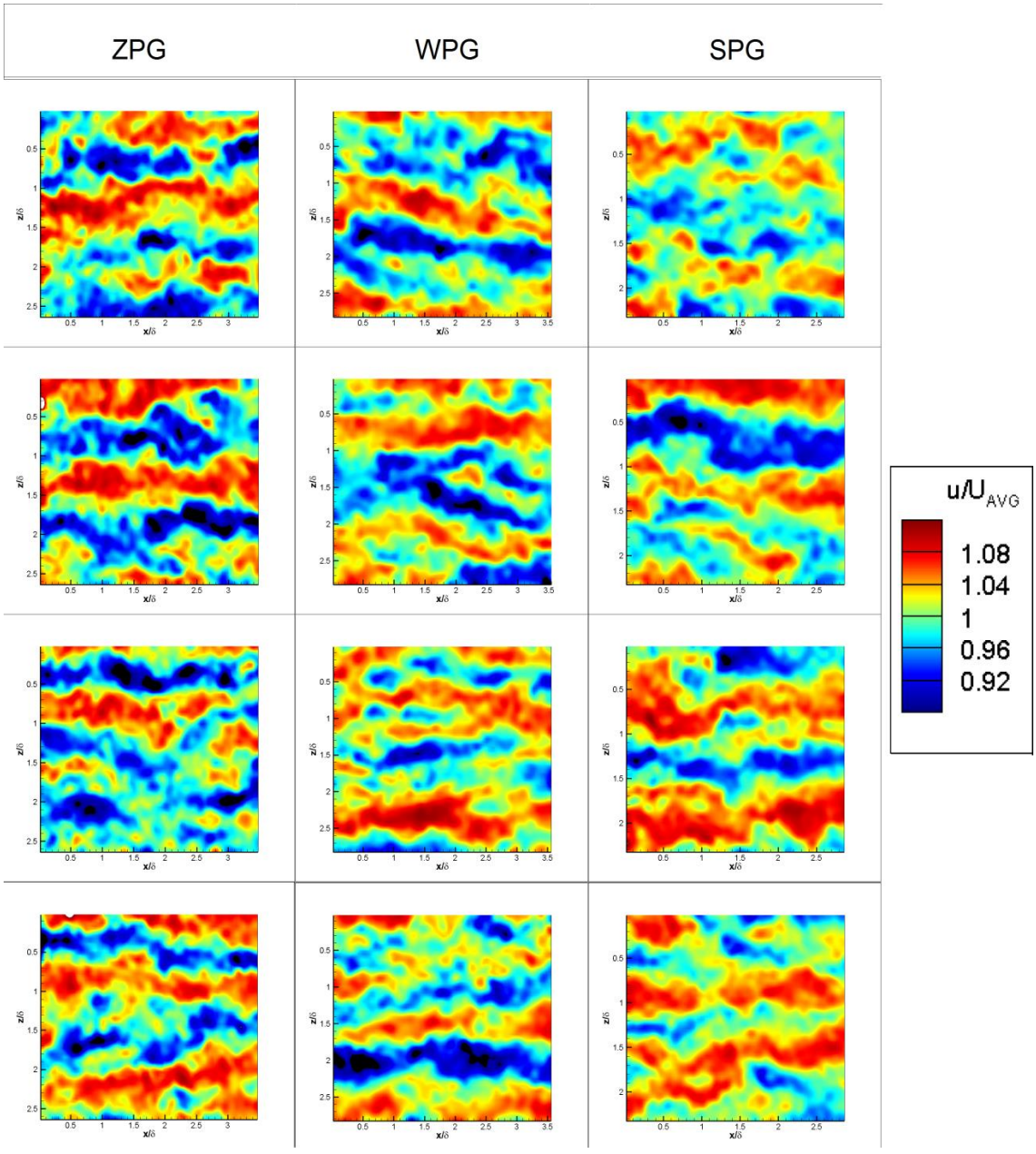

Fig. 20: Instantaneous velocity field comparison at $y/\delta \approx 0.5$.

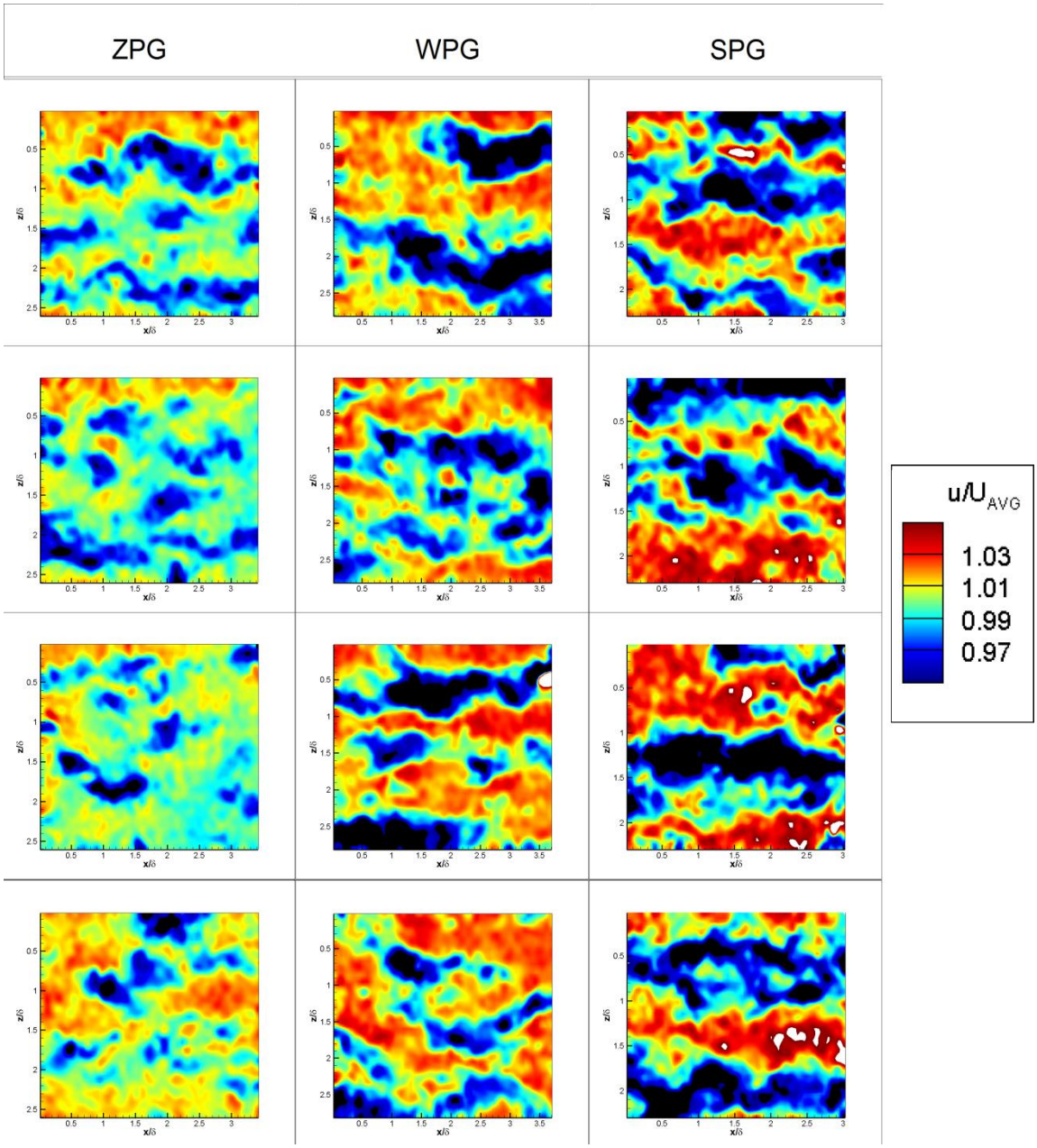

Fig. 21: Instantaneous velocity field comparison at $y/\delta \approx 0.9$.

The difference in the intensity and organization of the high and low speed velocity structures is readily apparent between the ZPG and SPG at the $y/\delta \approx 0.2$ and

0.9 locations. However, the spanwise/streamwise distribution and organization of the turbulence structures is less apparent. Also, Figures 19-21 deal with a very small sample size, chosen only to roughly represent the difference in large-scale turbulence structure behavior between the three pressure gradient models. In order to get a more accurate representation of the overall turbulence structure behavior of each test condition, the statistical autocorrelations is examined.

Figure 22 shows typical autocorrelation profiles representing streamwise-elongated turbulent structure behavior taken by Ganapathisubramani [11] at $y/\delta = 0.16$ and $M = 2$. In these autocorrelations, a higher, wider profile represents structural sizes which are statistically correlated over longer distances, i.e., larger or better organized structures. Streamwise elongated structures are marked by long tailed profiles in the R_{ux} correlation and sharp, narrow profiles in the R_{uz} correlation. Distinct profile inversions in the R_{uz} correlation represent alternating high and low speed velocity bands at regular intervals in the spanwise direction throughout the data set. The width of the profile in the streamwise or spanwise correlation represents the statistical distribution of size of the velocity region in each respective direction.

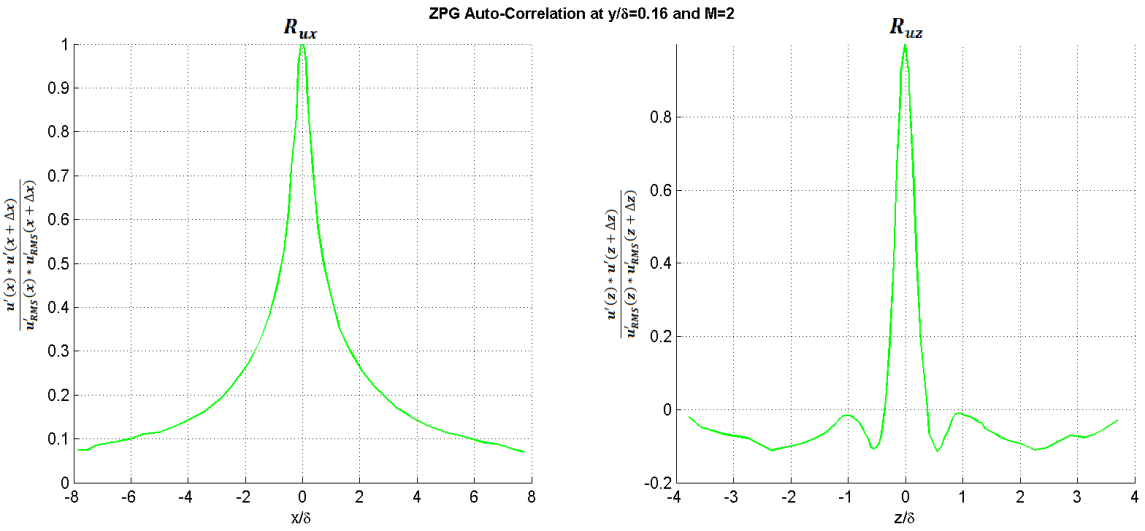

Fig. 22: Typical autocorrelation profiles for streamwise-elongated behavior. [11]

Figures 23 through 25 show the autocorrelation profile comparisons for each pressure gradient model at $y/\delta = 0.2$, 0.5, and 0.9 respectively. For ease of comparison, please note that each pressure gradient and boundary layer height location has a specific color and line-type in the autocorrelation profiles, which remain constant throughout the various figures.

At the $y/\delta \approx 0.2$ location in Figure 23, R_{ux} becomes decreasingly correlated from the ZPG to the SPG test case. For R_{uz}, the ZPG and WPG case have nearly the same correlation, while the SPG profile is narrower with a shallower inversion. This indicates structures in the SPG case which are statistically shorter in the streamwise direction, and narrower in the spanwise direction than found in the ZPG or WPG case. This also shows that the spanwise high and low speed structures are not as regularly spaced in the SPG case as they are in the ZPG or WPG. These profiles agree with the physical phenomenon that can be seen in the instantaneous images shown in Figure 19

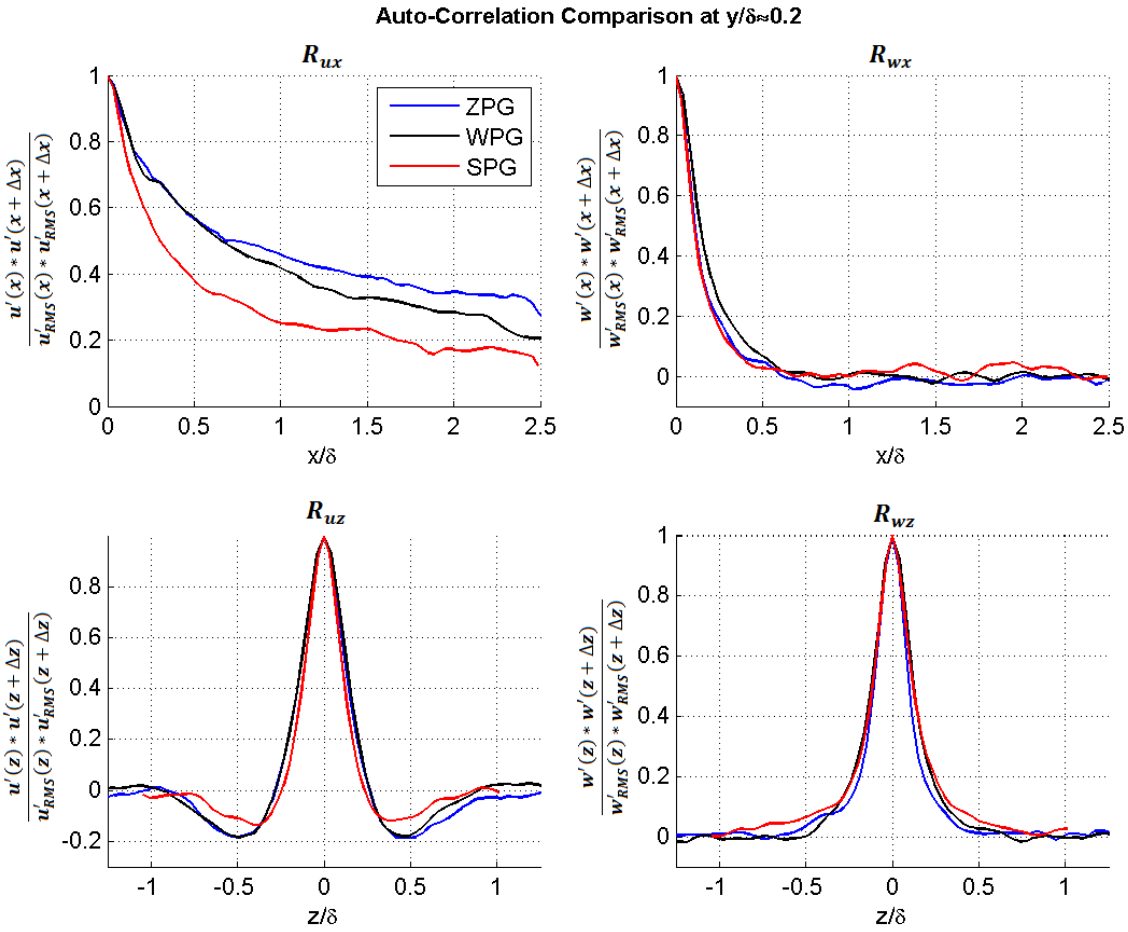

Fig. 23: Autocorrelation profiles comparison at $y/\delta \approx 0.2$.

and the separate instantaneous series video files. Notice also that there is very little variation in the R_{wx} or R_{wz} between the different pressure gradients at this height. This happens to be the case for all boundary layer heights and models tested in this study.

Figure 24 shows the same pressure gradient auto-correlation profile comparison at the $y/\delta \approx 0.5$ location. The ZPG has a significantly wider R_{ux} profile compared to the other pressure gradients. However, the ZPG, WPG, and SPG show very little relative variation in the R_{uz} profile. The SPG R_{uz} profile shows the same slightly narrower behavior as the $y/\delta \approx 0.2$ location, however, the magnitudes of the inversions in the

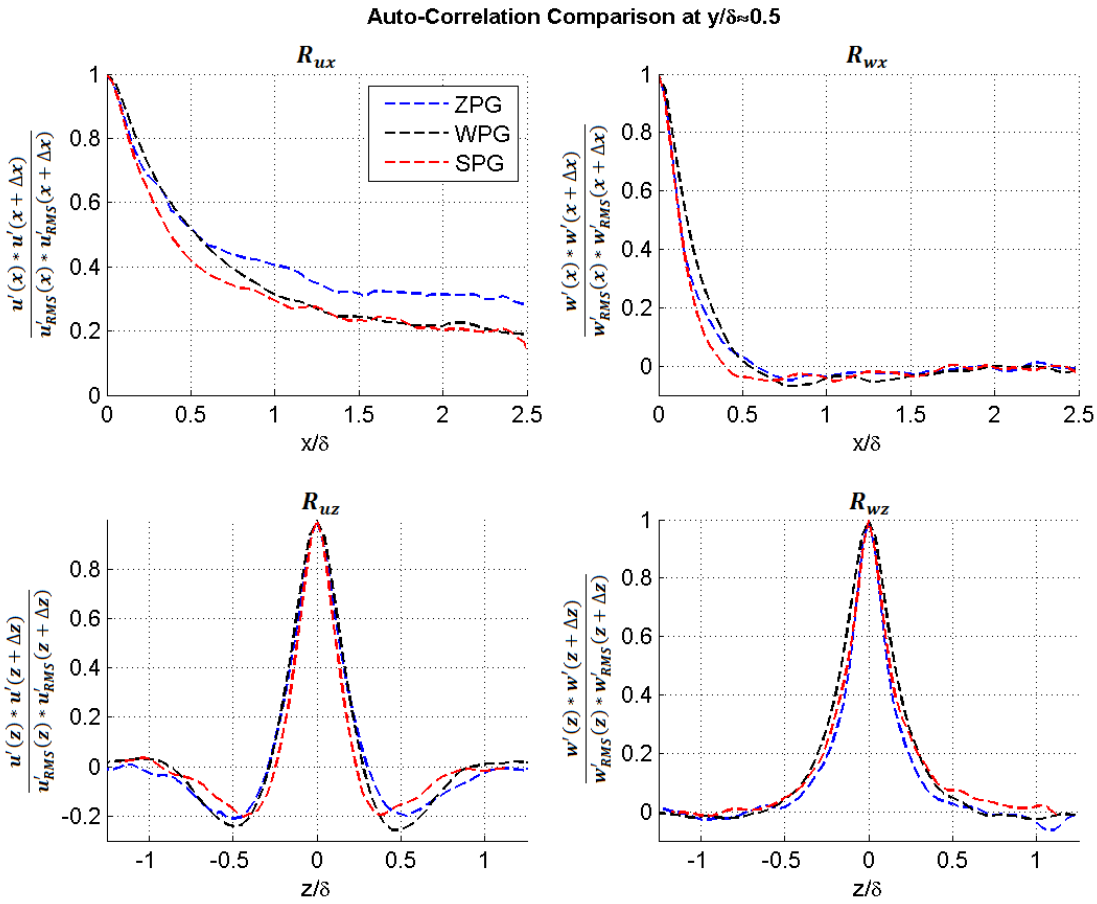

Fig. 24: Autocorrelation profiles comparison at $y/\delta \approx 0.5$.

three profiles are not significantly different from each other. Once again, these results agree with the visual analysis from Figure 20 and the compiled video files.

The autocorrelation profiles for the $y/\delta \approx 0.9$ location are shown in Figure 25. At this boundary layer height, the difference between the correlation profiles for R_{ux} is less than seen in the $y/\delta \approx 0.2$ or 0.5 locations, even though the ZPG case still exhibits more correlation at longer distances. However, there is a noticeable difference in the R_{uz} profile. The SPG now exhibits the strongest spanwise correlation behavior. It is still narrower than the other two profiles, but now exhibits a much sharper inversion,

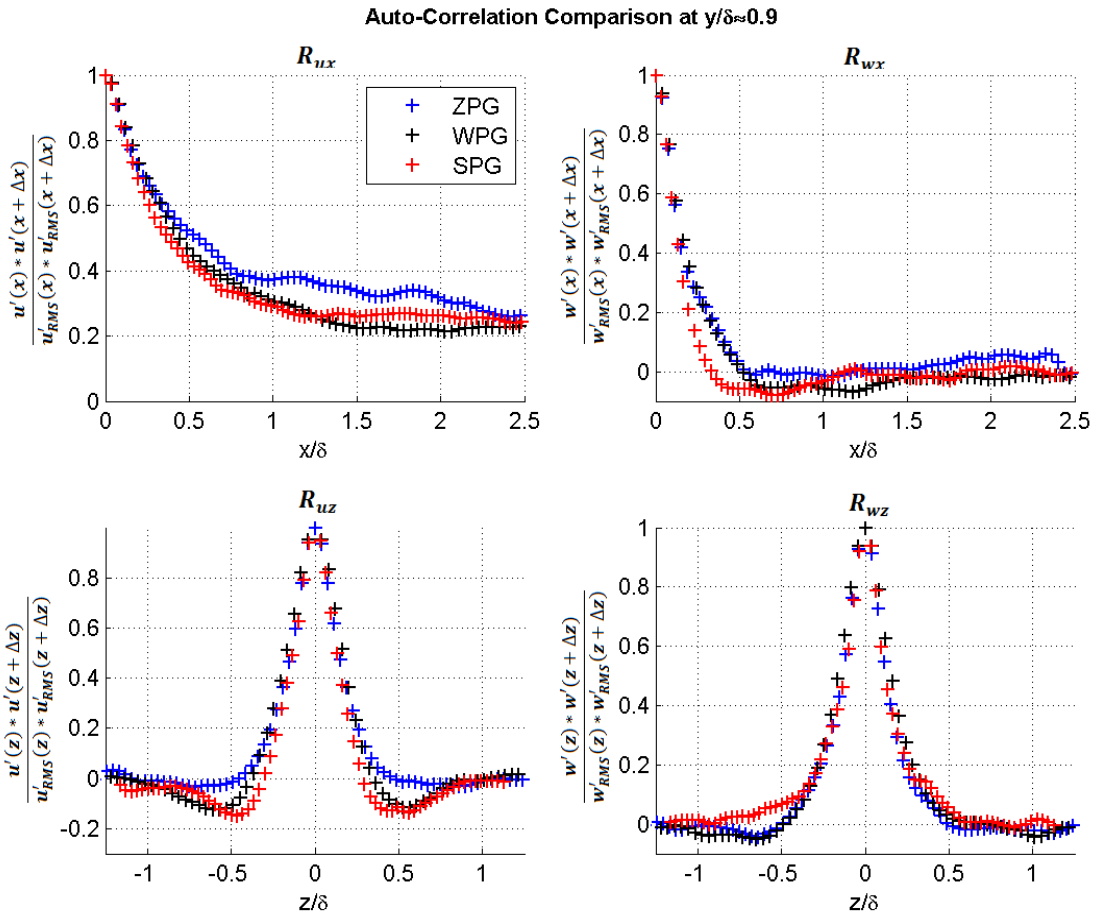

Fig. 25: Autocorrelation profiles comparison at $y/\delta \approx 0.9$.

particularly when compared to the ZPG case. The R_{wx} and R_{wz} correlation profiles still show very little change between pressure gradients.

Figure 26 shows the R_{wx} and R_{wz} profiles for every pressure gradient and boundary layer height tested. The only notable difference in the correlations is a slight narrowing of the R_{wx} profile in the SPG compared to the ZPG and WPG data. Given the standard correlation cutoff of 0.1, the statistical size of the W correlation lies within the range of $0.5 - 0.75\delta$ for R_{wx}, and 0.75δ for R_{wz}. This correlation size appears to be

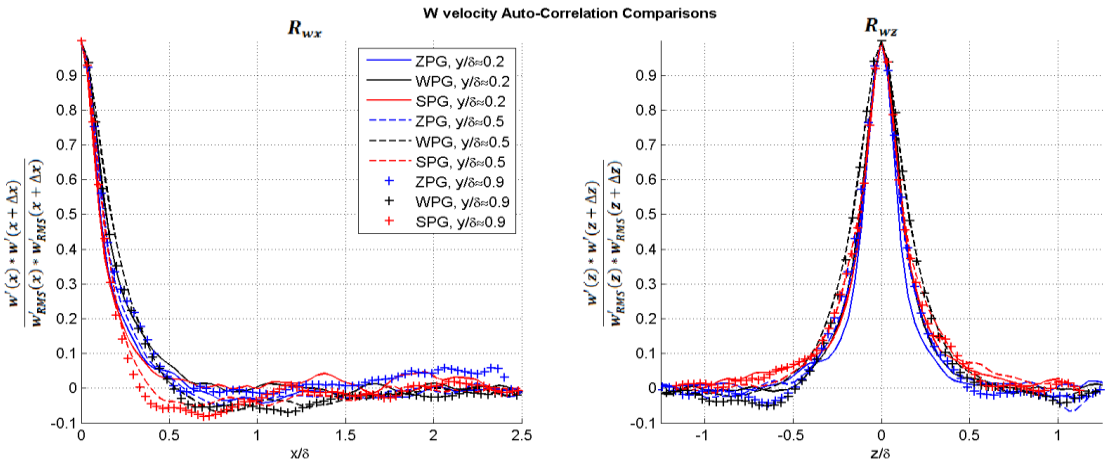

Fig. 26: W Autocorrelation profiles comparison at all test locations.

almost completely independent of pressure gradient or boundary layer height across the range tested.

As previously mentioned, the R_{ux} profiles represent a general trend in which the large scale turbulence behavior continuum shifts from ZPG-WPG-SPG at the lower boundary layer height to SPG-WPG-ZPG at the upper boundary layer height, in order from strongest to weakest. This corresponds with the trend shown in Figures 14 and 15, where ${u'}_{RMS}$, ${w'}_{RMS}$, TKE, $\overline{u'u'}$, $\overline{u'w'}$, & $\overline{w'w'}$ are all significantly less for the SPG at the lower boundary layer heights, roughly equivalent for the three pressure gradients at the middle boundary layer height, and slightly higher for the SPG at the upper boundary layer height. This trend is mimicked by the R_{uz} correlations shown in Figures 23, 24, and 25, corresponding with the visual analysis discussed earlier.

Figure 27 shows the R_{ux} and R_{uz} profiles for all boundary layer heights tested for the ZPG, WPG, and SPG models respectively. Notice that for all three pressure

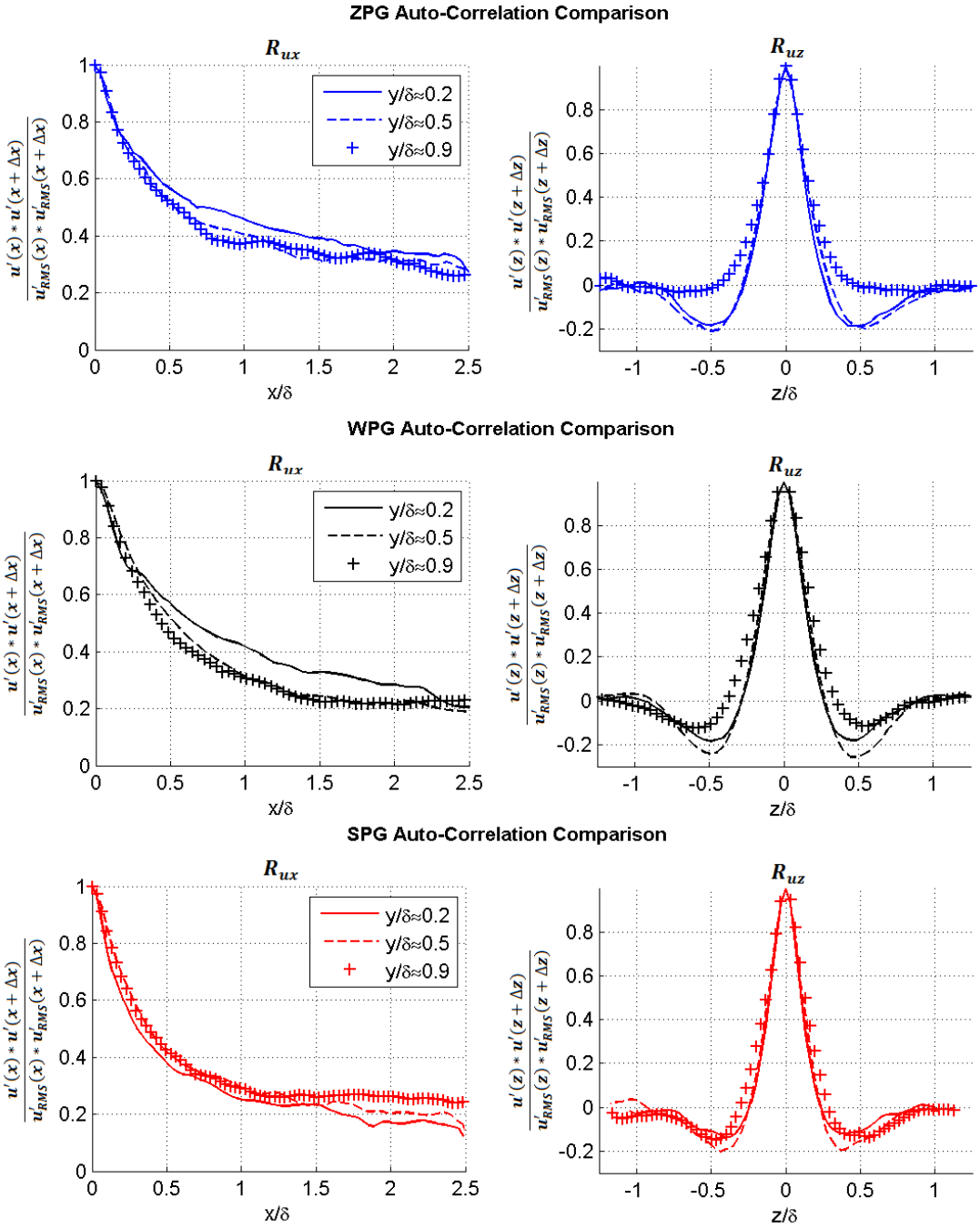

Fig. 27: *U* autocorrelation profiles comparison vs. boundary layer height.

gradients, the R_{ux} profile is mainly independent of boundary layer height. However, the R_{uz} profile is only independent of boundary layer height for the SPG case. The ZPG and WPG both exhibit behavior in which the R_{uz} profile is dependent on boundary layer height. The ZPG shows the strongest dependence on boundary layer height of the three pressure gradients tested. Although the ZPG R_{uz} profiles for the $y/\delta \approx 0.2$ and 0.5 cases are very similar, the $y/\delta \approx 0.9$ profile has lost all of its spanwise inversion. The WPG shows more distributed behavior, where the $y/\delta \approx 0.5$ location exhibits the strongest spanwise inversion, and the $y/\delta \approx 0.2$ shows the least. This is similar to the behavior shown by the R_{uz} profile for the SPG case, but the differences in behavior between the boundary layer heights is much less pronounced for the SPG.

The correlation of the large scale turbulence structures in the SPG is relatively independent of δ. This results in milder streamwise-elongated behavior at the lower boundary layer heights compared to the ZPG and WPG profiles, where they are at or near their strongest behavior. However, in the upper boundary layer heights, where the ZPG and WPG structures have lost much of their correlation, the SPG appears stronger in comparison. This corresponds with the visual analysis from Figures 19-21.

When calculating the autocorrelation profiles, three locations along the $x - axis$ were considered: the upstream edge of the field of view, the center of the field of view, and the downstream edge of the field of view. For most cases, little to no variation between the correlation profiles was exhibited between the three locations. However, this was not the case for the SPG case at the lower boundary layer height. Figure 28 shows the autocorrelation profiles calculated for the upstream and downstream edges of

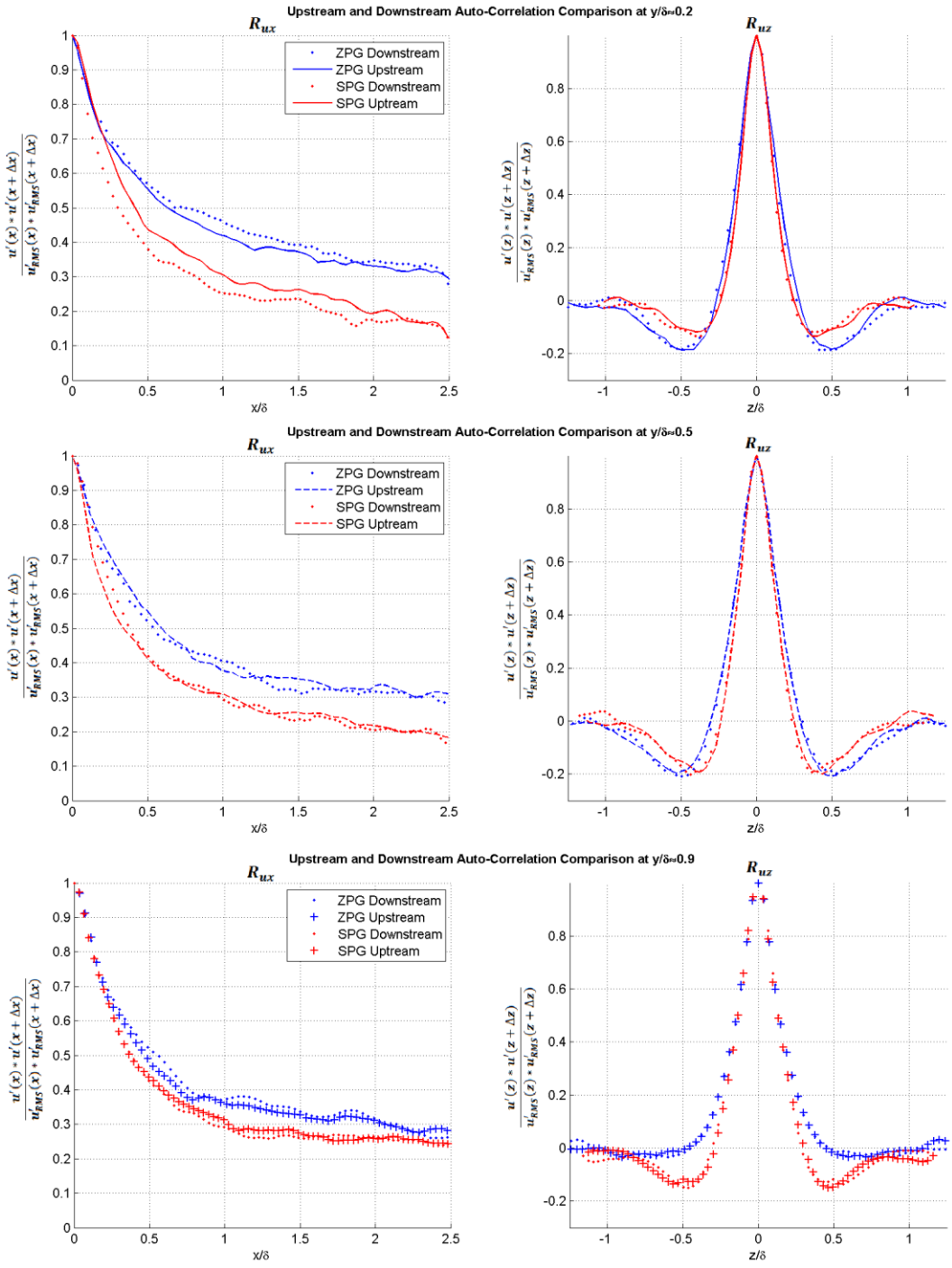

Fig. 28: Upstream and downstream U autocorrelation profiles comparison.

the field of view for the ZPG and SPG at all three boundary layer heights. The dotted lines in the figures show the autocorrelation profiles calculated at the downstream edge of the field of view. The autocorrelation profiles calculated for the upstream edge of the field of view use the same colors and symbols as the autocorrelation profiles shown earlier. The streamwise distance between the two autocorrelation profiles for each case is approximately 3δ.

In Figure 28, it can be seen that the R_{ux} autocorrelation profile for the SPG at the $y/\delta \approx 0.2$ location drops significantly between the upstream and downstream edges of the field of view. However, the spanwise R_{uz} correlation at this location appears to be completely independent of streamwise location in the field of view. This also appears to be the case for both the R_{ux} and R_{uz} correlation profiles for the $y/\delta \approx 0.5$ and $y/\delta \approx 0.9$ locations.

A further effort was made to determine the streamwise dependence of the SPG R_{ux} correlation profiles at the lower boundary layer height. For this analysis, a new correlation parameter was used, the R_{ux} correlation distance. This is the distance in the streamwise direction from the correlation origin that it takes for the correlation coefficient to reach half of its original value. This represents the streamwise width of large-scale structures which are statistically correlated to a value of 0.5. For locations and test conditions which are independent of streamwise location, this value should remain constant. If this value shows significant variation in the streamwise direction, it indicates a streamwise location dependence on the height and width of the R_{ux}

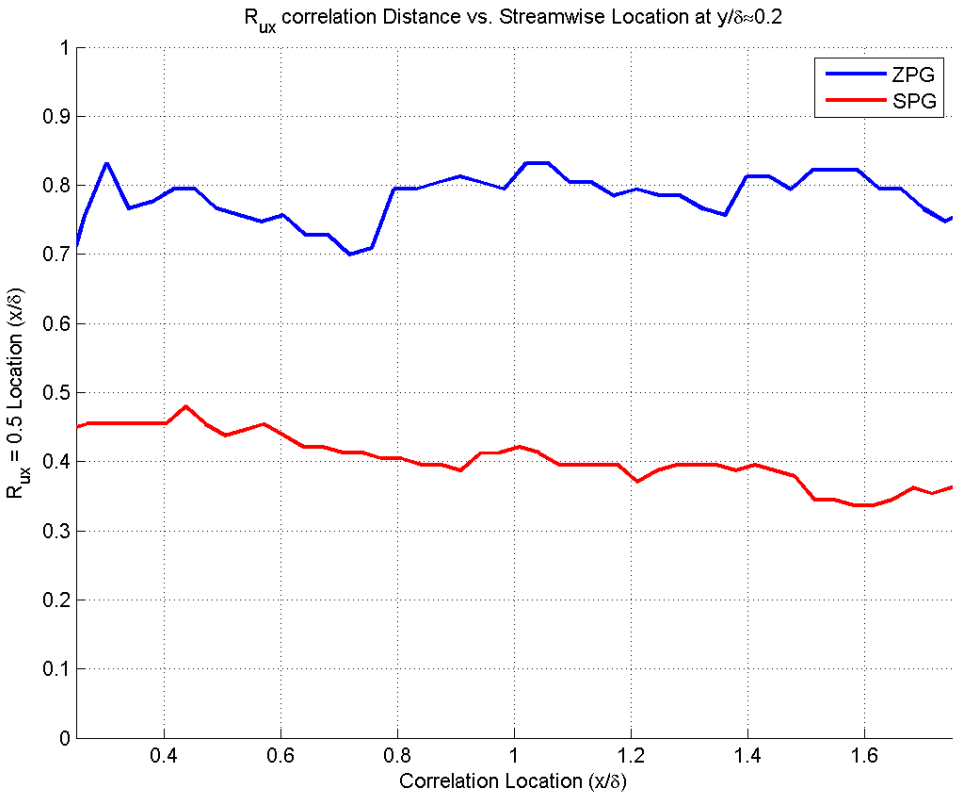

Fig. 29: R_{ux} correlation distance comparisons at $y/\delta \approx 0.2$.

autocorrelation profile, and thus the statistical streamwise length of the large-scale turbulence structures.

Figure 29 shows the R_{ux} correlation distance comparison for the ZPG and SPG at the $y/\delta \approx 0.2$ location. Notice that the $R_{ux} = 0.5$ location remains essentially constant for the ZPG case, with a value of approximately $0.8\,x/\delta$. However, for the SPG case, the $R_{ux} = 0.5$ location shows a decreasing trend from the upstream edge of the field of view to the downstream edge. The R_{ux} correlation distance drops from a value of approximately $0.45\,x/\delta$ to approximately $0.35\,x/\delta$ over a streamwise distance of 1.8δ. This represents a decrease in streamwise correlation distance of approximately

22% over a relatively short streamwise distance. This trend further helps identify the streamwise development of the large-scale turbulent structures, notably their decrease in statistical streamwise length as the flow progresses over the SPG model.

In order to further quantify the relative intensities of the large scale turbulence structures over the different favorable pressure gradients, a new series of autocorrelation profiles were calculated. Unlike the previous autocorrelations, which were normalized by the local u'_{RMS} and w'_{RMS} values, these new autocorrelations were non-dimensionalized by a reference U-velocity variable, $U_{ref} = 750m/s$. This value was chosen to approximate the average free stream velocity of the different test cases. By non-dimensionalizing the autocorrelations instead of normalizing them, the relative intensity of the high and low speed turbulence structures is quantified by the respective heights of the autocorrelation profiles near the $x/\delta \ or \ z/\delta = 0$ location.

Figure 30 shows the non-dimensionalized autocorrelation profiles for each of the pressure gradients and boundary layer heights tested. It is clearly evident that the SPG structures exhibit much less intensity in both the R_{ux} and R_{uz} correlations at the $y/\delta \approx 0.2$ location, as was seen in the visual analysis earlier. At the $y/\delta \approx 0.5$ location, the difference is less pronounced, although the SPG is still weaker than the other two pressure gradients. However, at the $y/\delta \approx 0.9$ location, the SPG correlation profile is slightly higher, indicating relatively high turbulence structure velocity intensity. The non-dimensional correlation profiles at all three boundary layer height locations support

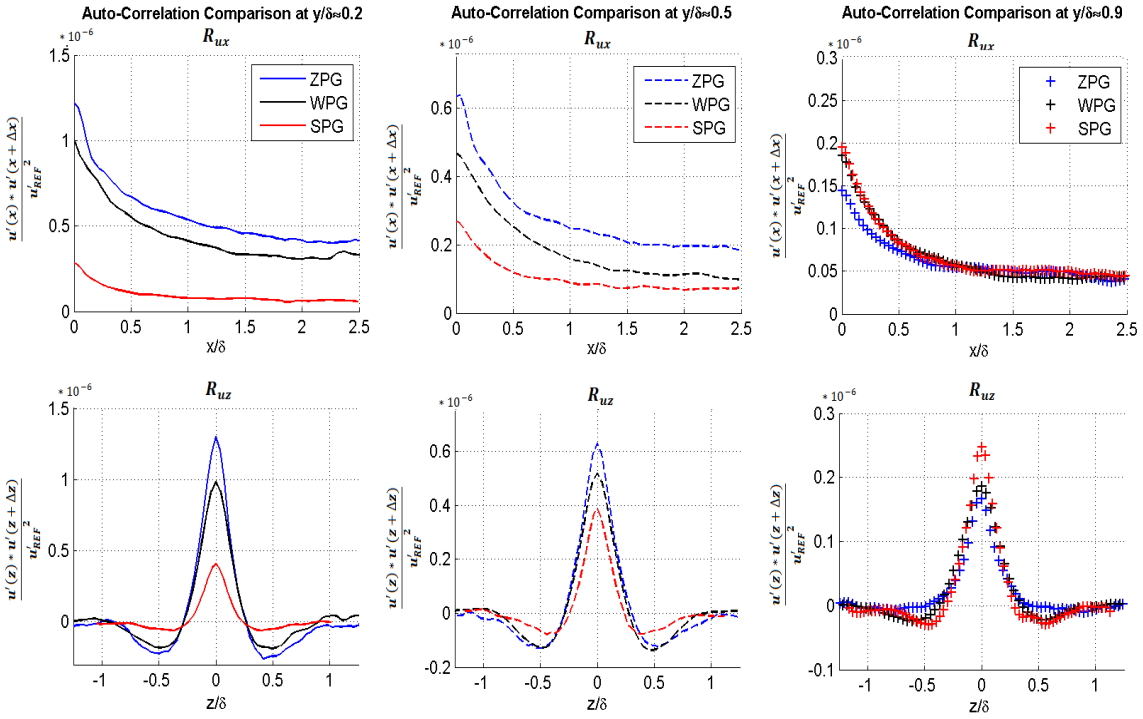

Fig. 30: Non-dimensionalized autocorrelation profile comparisons.

the trends described earlier in the visual instantaneous image analysis.

The mechanisms that drive the unique behavior in the SPG case cannot be determined from the data collected for this study. One possible explanation is the dilatation that must take place due to the physical expansion experienced in the test section environment and the compressibility inherent in the current test conditions. As the airflow negotiates the strong favorable pressure gradient, large scale structures in the boundary layer are expanding. It is possible that this expansion is causing the structures to spread to regions of the boundary layer where they are not so prevalent under a zero or weak favorable pressure gradient. Regardless of the mechanism involved, the behavioral independence from boundary layer height location in the strong favorable

pressure gradient case may be one of the most important findings of this study. The matching trend between the statistical correlation and structural behavior of the pressure gradients and their respective TKE and Reynolds shear stress components is also another very important finding. This trend may prove a way of estimating large scale turbulence structure behavior for different flowfields based upon data that has already been gathered for them.

D. Mach Number Effects

Due to the similarities of the current study and the work conducted by Ganapathisubramani [11] on streamwise-elongated turbulence structures at $M = 2$, a comparison of the two studies provides interesting insight into the possible Mach number dependency of these types of structures. Figure 31 shows Ganapathisubramani's R_{ux} and R_{uz} autocorrelation profiles [11] at $M = 2$ for the $y/\delta \approx 0.2$ and 0.5 locations, as well as the autocorrelations computed for the current study. The R_{ux} profiles are very similar for both boundary layer height locations, suggesting the streamwise length of the large scale turbulence structures is mostly independent of Mach number. The R_{uz} profiles at the $y/\delta \approx 0.2$ location are also strikingly similar. Most notably, the statistical spanwise width of the structures appear to be virtually identical for both tests at this location, again suggesting an independence of Mach number for the spanwise condition in the lower boundary layer region. The biggest difference between the results of the two studies is seen in the R_{uz} profiles at the $y/\delta \approx 0.5$ location. It would appear that the higher Mach number in the current study is causing the sharp spanwise orientation of the

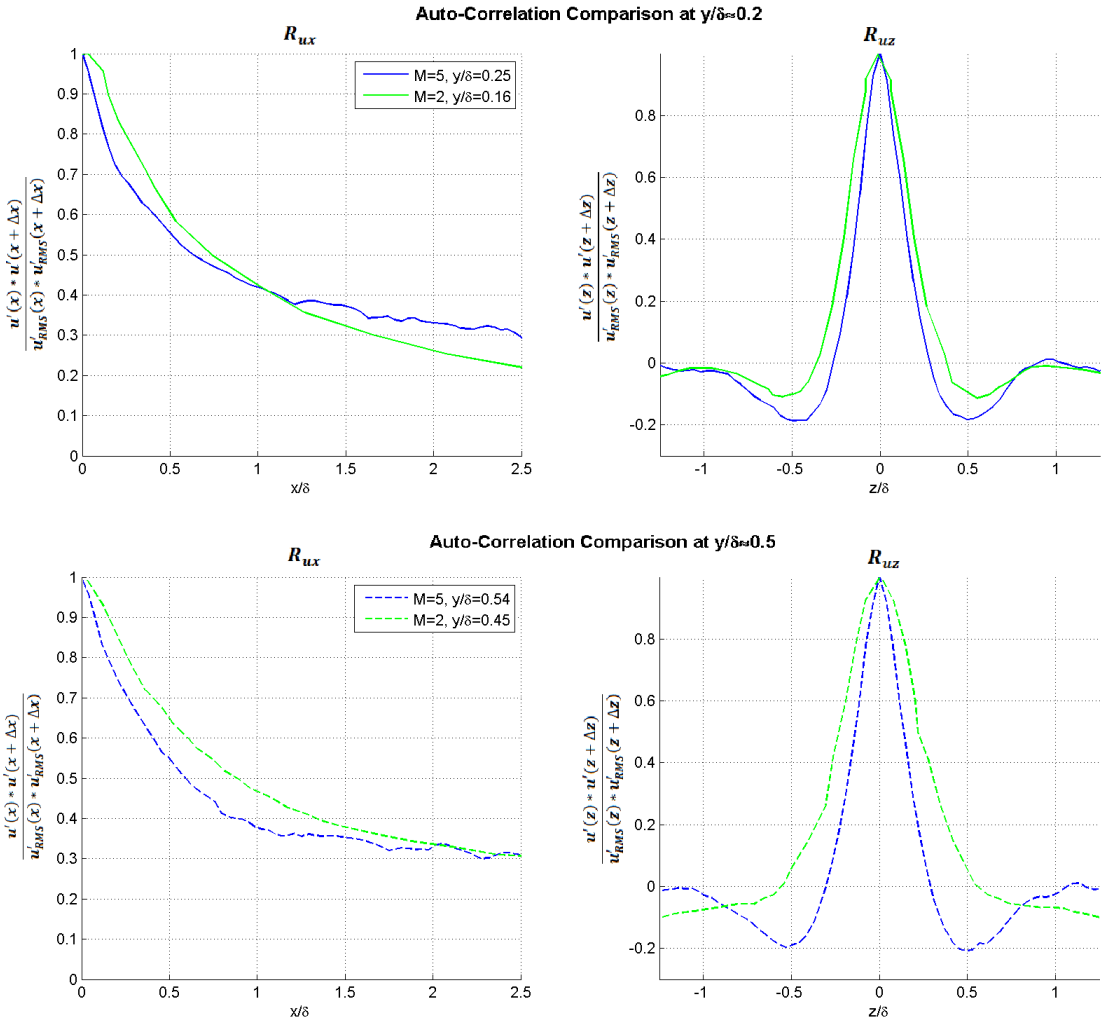

Fig. 31: U autocorrelation profiles comparison at $M = 2$ and $M = 5$. [11]

high and low speed structures to move upwards in the boundary layer compared to the $M = 2$ case. As a general trend, the large-scale structures appear to maintain their streamwise length while becoming narrower and more pronounced in the spanwise direction as Mach number increases. This trend is mirrored in Figure 32 by the R_{wx} and R_{wz} correlation profiles for the same Mach number comparison. Notice that for both

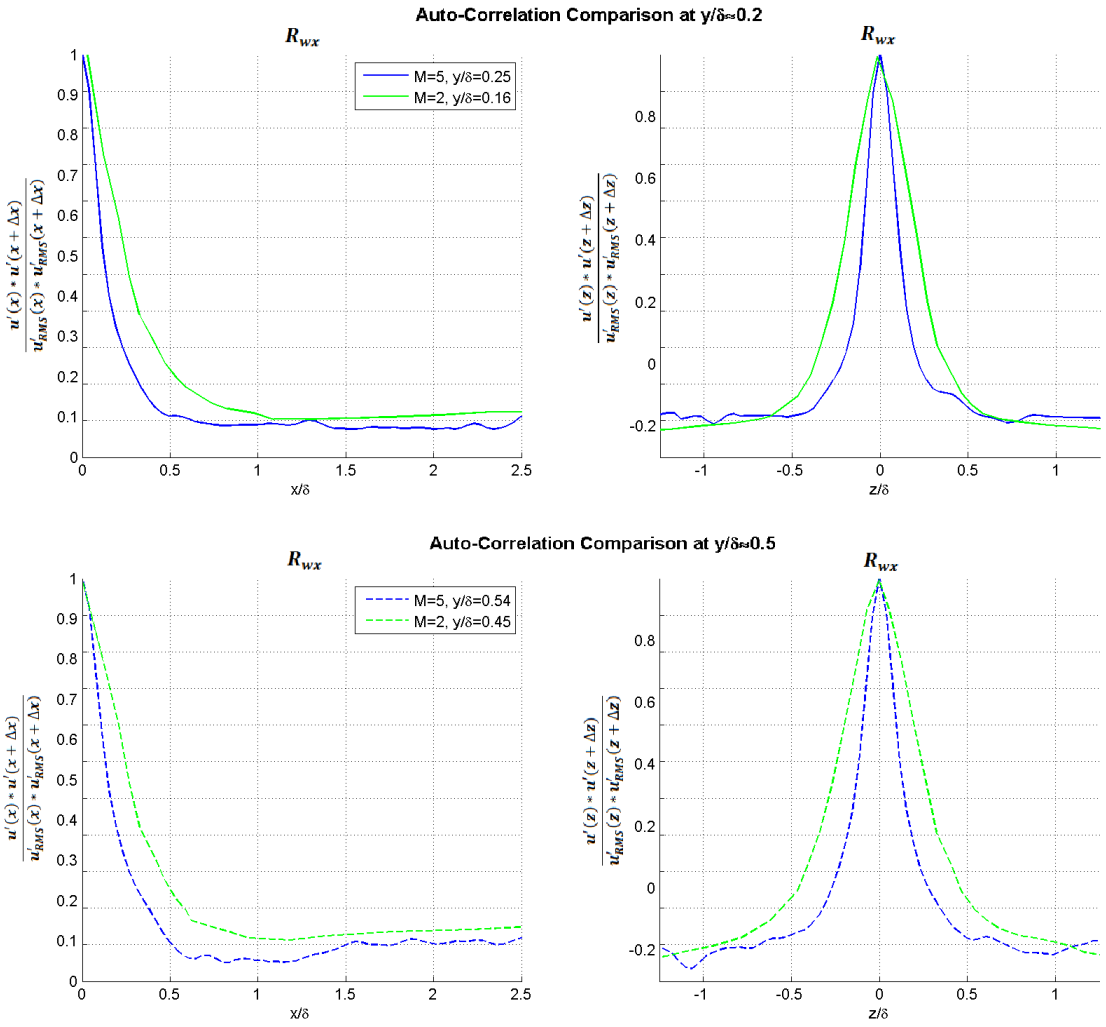

Fig. 32: W autocorrelation profiles comparison at $M = 2$ and $M = 5$. [11]

boundary layer height locations, the W correlation profiles are the same shape, but slightly narrower in the streamwise and spanwise distances. This also points towards a narrowing spanwise large-scale turbulent structure size at higher Mach numbers. However, the dependency does not appear to be very strong, as more than doubling the Mach number only results in a slight narrowing of the correlation profiles.

E. Roughness Element Effects

Information about the size, distribution, and intensity of large-scale turbulence structures can also be gained from viewing instantaneous images of the velocity vector fields for the roughness element flat plate comparisons. Figures 33-35 show the randomly selected instantaneous vector fields from the RZPG case compared to the ZPG case for the $y/\delta \approx 0.2,\ 0.5$, and 0.9 cases. These images use the same velocity percentage bands and coloring scheme as described for Figures 19-21.

Figure 33 shows the lower boundary layer height location. Notice that the difference in the magnitude of the velocity of the high and low speed regions is much greater for the RZPG case. However, even though the relative velocity differences are greater, the structures are not as well defined along the streamwise elongated pattern. Not only are they more broken in the streamwise direction, they also appear to be less aligned with the x-axis, and are narrower with sharper contrasts in the spanwise direction.

Similar to the favorable pressure gradient cases, the middle boundary layer height shows a sharp decrease in the constrast between the relative velocity intensities of the two models. As shown in Figure 34, the relative intensities between the ZPG and RZPG case at the $y/\delta \approx 0.5$ location are approximately equal. There also appears to be less difference in the spanwise and streamise size and orientation of the structures at the $y/\delta \approx 0.5$ location. This is very similar to the behavior seen in Figure 35 at the upper boundary layer height. However, there does appear to be an increase in the magnitude of

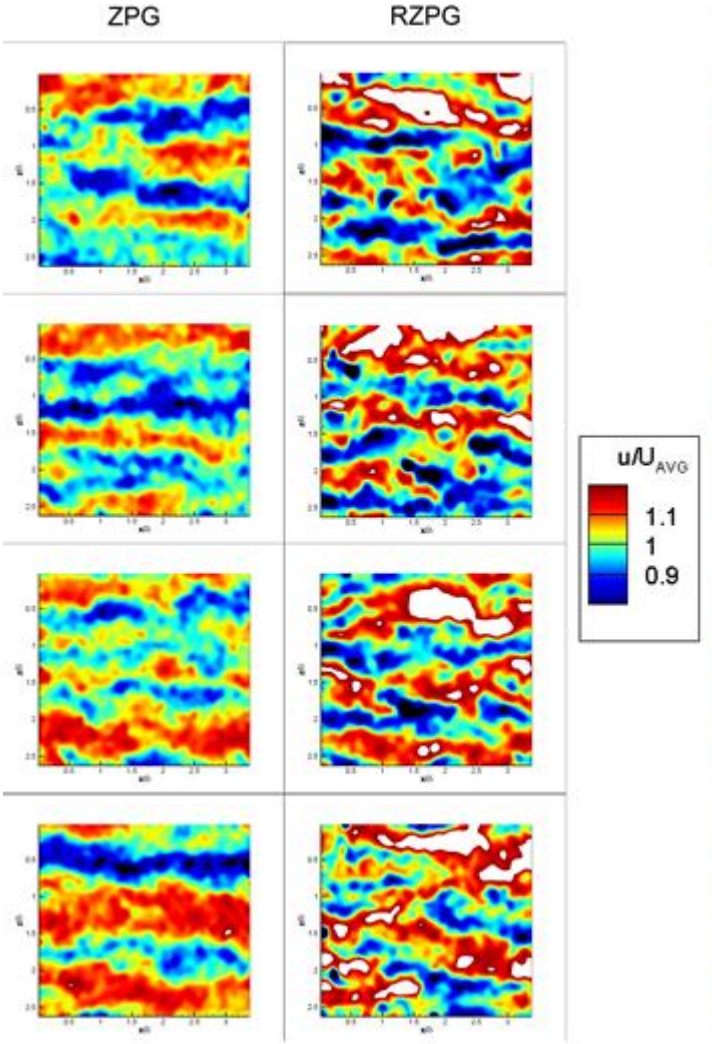

Fig. 33: Instantaneous velocity field comparison at $y/\delta \approx 0.2$.

the relative velocities of the structures in the RZPG case compared to the ZPG images. This increase in strength is also visible in the video files, although it is not quite as apparent as in the instantaneous image files shown here. This is most likely an effect of the RZPG measurements actually being taken 10-15% lower in the boundary layer than the earlier ZPG measurements, as shown in Table 5 of Chapter III. The intesnity of all

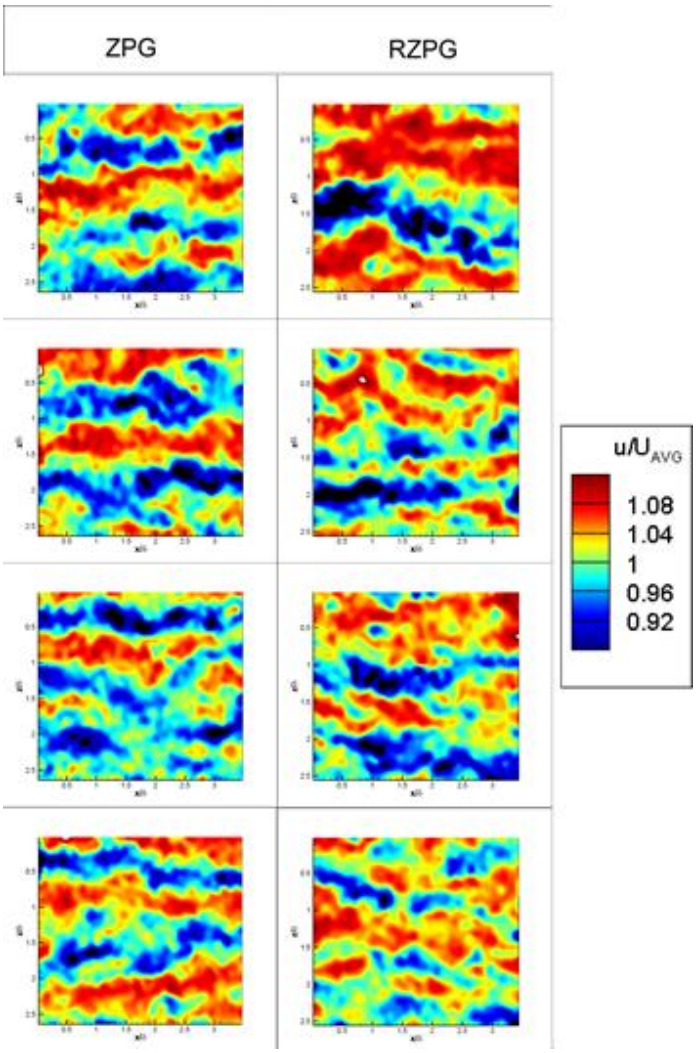

Fig. 34: Instantaneous velocity field comparison at $y/\delta \approx 0.5$.

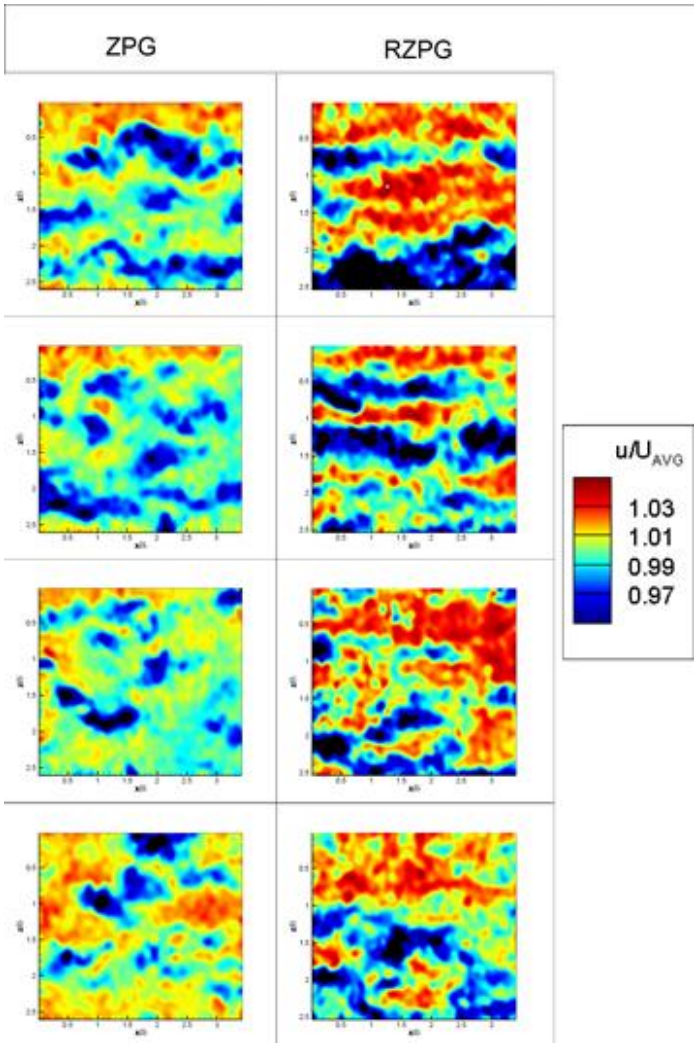

Fig. 35: Instantaneous velocity field comparison at $y/\delta \approx 0.9$.

the test cases was inversely proportional to boundary layer height. Therefore, the higher y/δ location of the ZPG case likely is driving the trend of lesser intensity seen in Fig 35 and the video files.

Figures 36-38 show the autocorrelation profiles of the ZPG and RZPG cases at $y/\delta \approx 0.2$, 0.5, and 0.9. In these figures, the RZPG take the red color previously assigned to the SPG case in the favorable pressure gradient comparisons.

Comparing the correlations in Figure 36 at the $y/\delta \approx 0.2$ location, it is readily apparent that the RZPG case has a much narrower R_{ux} profile than the ZPG case. This is also true of the $y/\delta \approx 0.5$ location, as is shown in Figure 37. The R_{uz} profile for the ZPG and RZPG at both of these boundary layer heights are very similar. The R_{uz} profile for the RZPG case is noticeably narrower than the ZPG at the lower boundary layer height, suggesting tighter spanwise structure distribution. However, this trend does not carry into the middle boundary layer height, where the R_{uz} profiles of both test cases are approximately the same width, with a bit shallower inversion seen in the RZPG case.

At the $y/\delta \approx 0.9$ location shown in Figure 38, the R_{ux} profile is still wider for the ZPG than the RZPG, but the difference is less pronounced than is seen at the lower boundary layer heights. The R_{uz} profiles between the two models are nearly identical at this upper boundary layer location, with the only visible difference being the slightly narrower behavior of the RZPG profile. This would suggest that the large-scale structures are very similar in streamwise length and spanwise width at this location. Note that although the two tests were taken at slightly different y/δ locations, the independence of spanwsie and streamwise correlation on boundary layer height for the

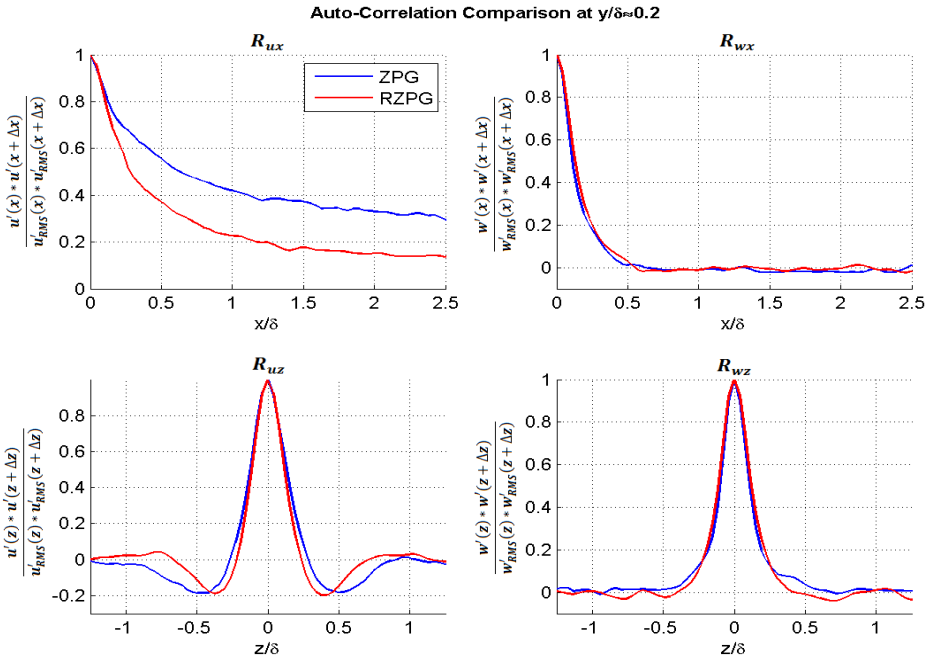

Fig. 36: Autocorrelation profiles comparison at $y/\delta \approx 0.2$.

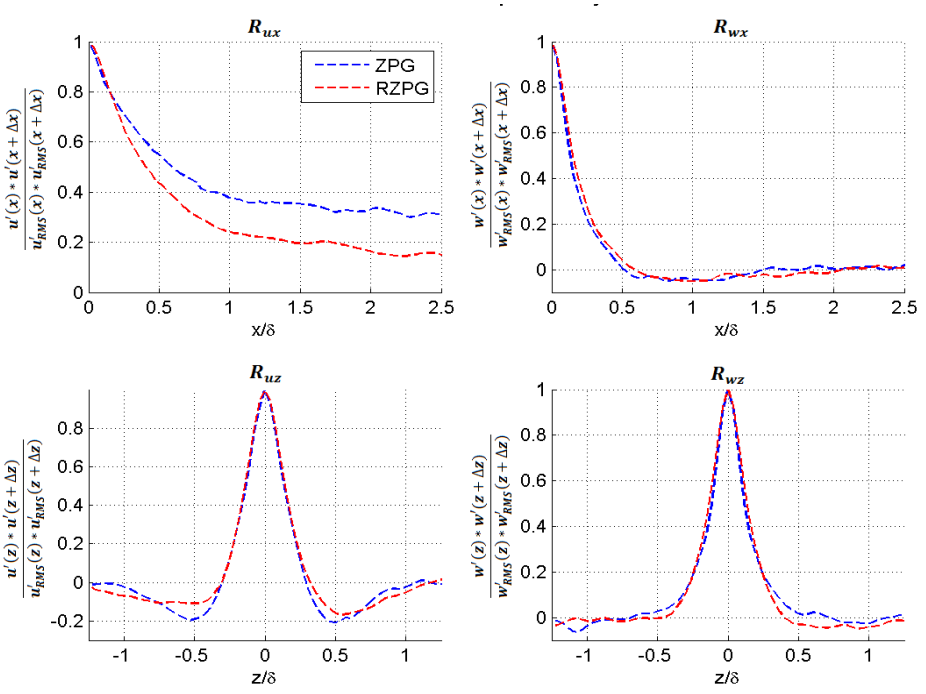

Fig. 37: Autocorrelation profiles comparison at $y/\delta \approx 0.5$.

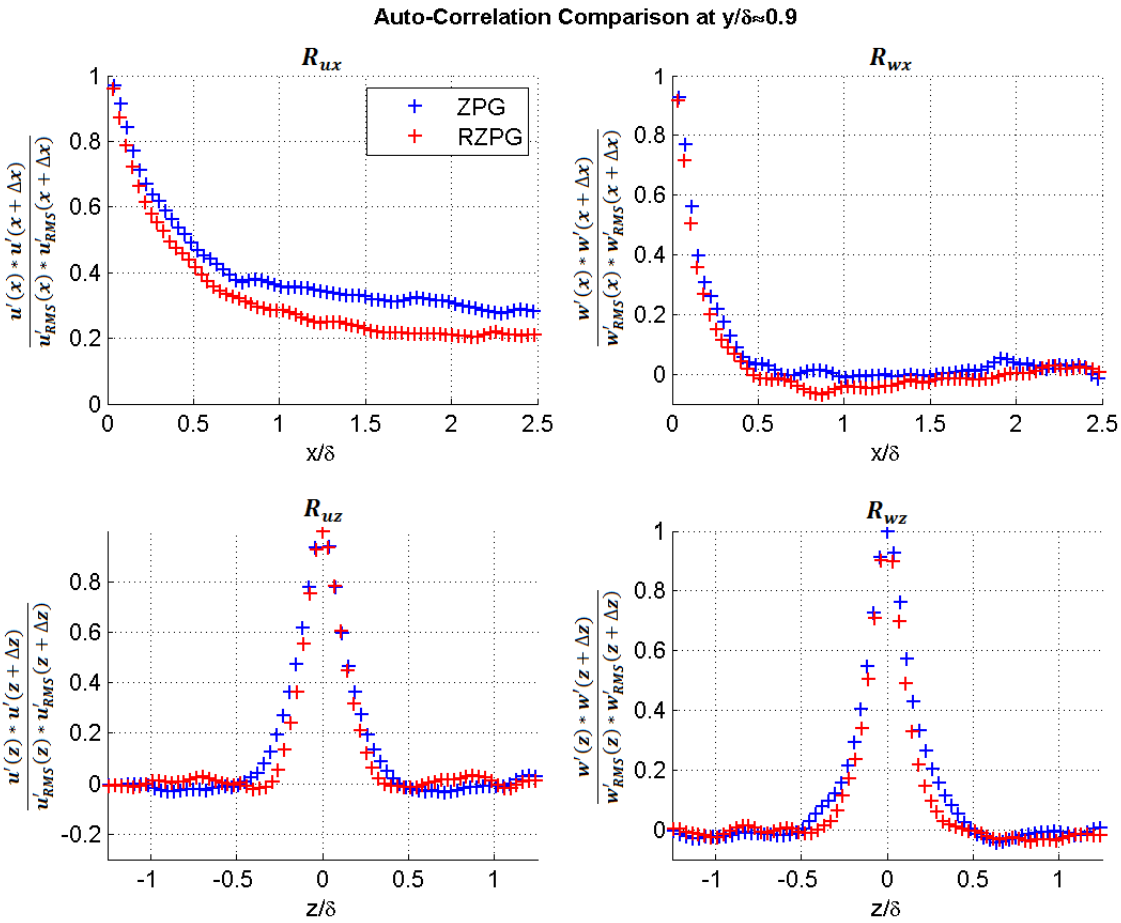

Fig. 38: Autocorrelation profiles comparison at $y/\delta \approx 0.9$.

respective pressure gradients this high in the boundary layer allows the autocorrelation to be an acceptable comparison between the two cases.

Notice that for all three boundary layer heights, the roughness elements have no apparent impact on the R_{wx} and R_{wz} profiles. This is the same result as was seen in the varying favorable pressure gradient comparison.

Figure 39 shows the change in the autocorrelation versus boundary layer height for the ZPG and RZPG conditions. Notice that similar to the pressure gradient

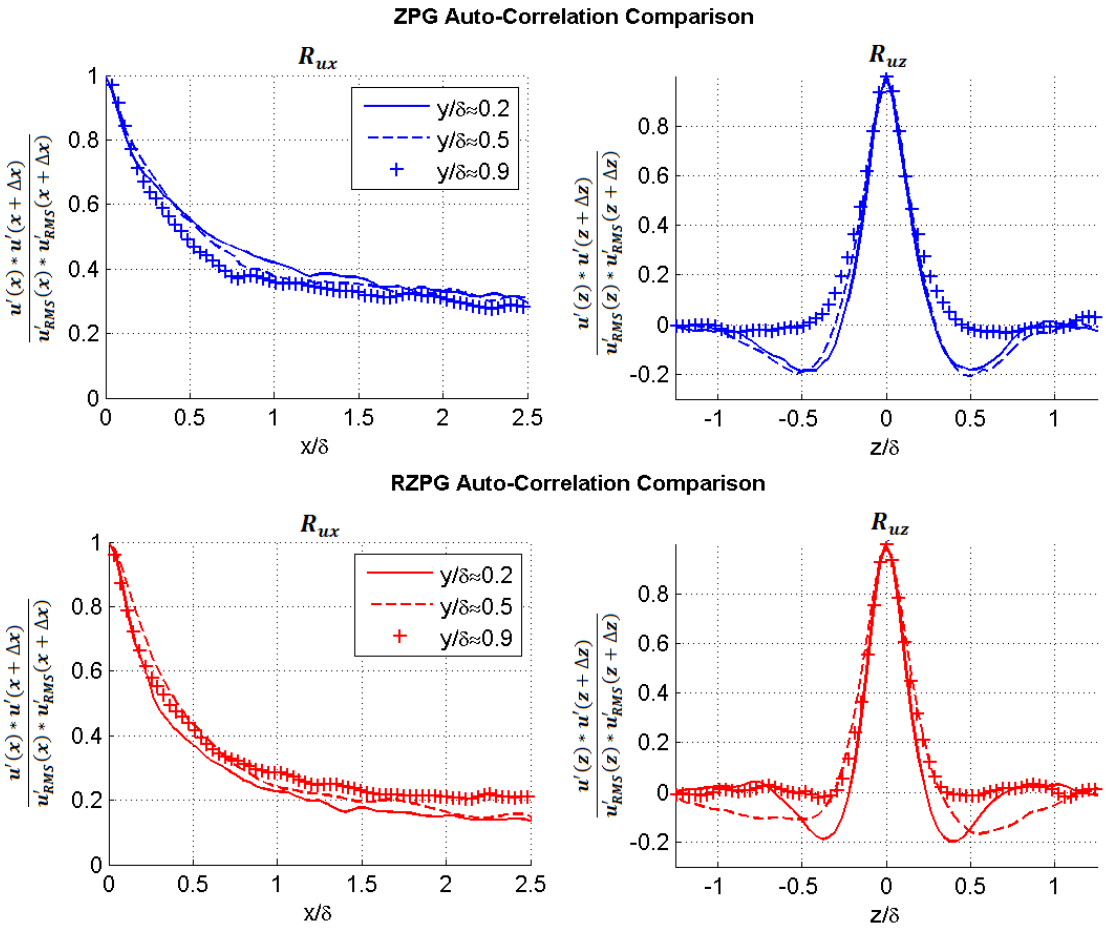

Fig. 39: Autocorrelation profiles comparison of ZPG and RZPG vs. $\boldsymbol{\delta}$.

comparison, change in boundary layer height has very little impact on the R_{ux} profile of the RZPG. However, it is also important to note that unlike the ZPG case, the RZPG case appears to become slightly more correlated at higher locations in the boundary layer. In both the ZPG and RZPG cases, the R_{uz} profiles demonstrate a similar trend from lower to upper levels of the boundary layer. The main difference between the two cases is a widening of the RZPG R_{uz} correlation profile between the $y/\delta \approx 0.2$ & 0.5 locations which is not present in the ZPG. Notice that the R_{uz} profile for the RZPG case

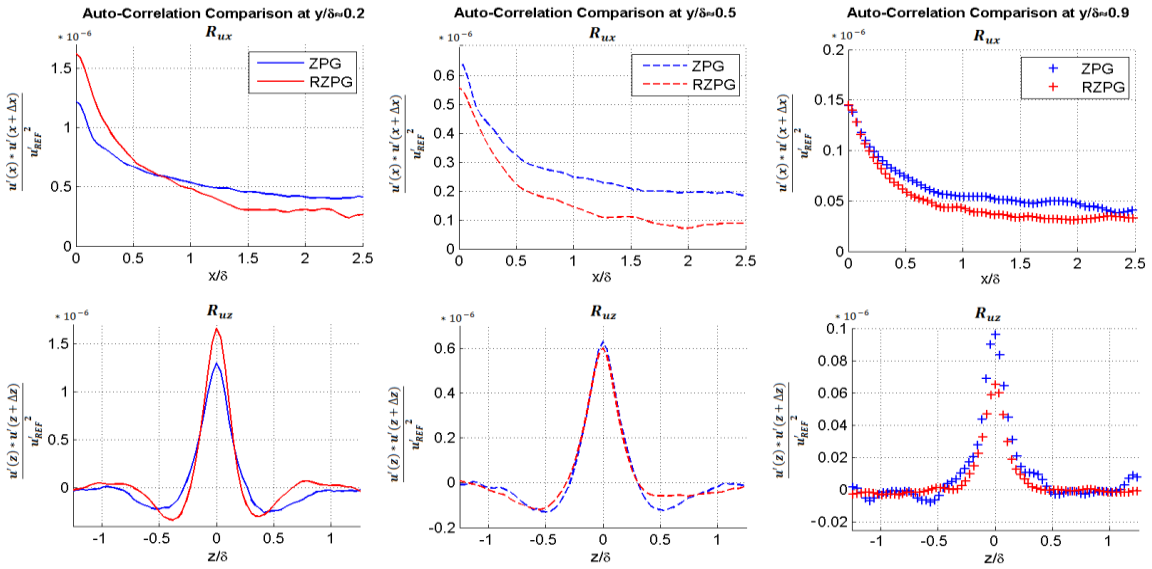

Fig. 40: Non-dimensionalized autocorrelation profiles comparisons.

at $y/\delta = 0.85$ is nearly identical to the ZPG case at $y/\delta = 0.98$. Since spanwise organization is inversely proportional to y/δ in these models, it can be assumed that the introduction of surface roughness elements is causing an absence of middle and upper boundary layer spanwise organization. It is also interesting to note that the change in the R_{ux} profile with respect to boundary layer height for the RZPG is very similar to that seen in the SPG profile shown in Figure 27.

Similar to the pressure gradient comparions shown earlier, a set of non-dimensionalized autocorrelation profiles were created for the surface roughness element comparison using the same U_{ref} value of $750\, m/s$ in order to compare the relative intensities of the high and low-speed structures. Figure 40 shows the non-dimensionalized autocorrelation comparisons for the ZPG and RZPG case at all three boundary layer heights.

Notice that at the $y/\delta \approx 0.2$ location, the height of the non-dimensionalized profile is greater for the RZPG case near the correlation origin. This shows a relative increase in the intensisty of the large-scale turbulence structures at the lower boundary layer height for the RZPG case, as was previously identified in the instantaneous image comparisons. However, the non-dimensionalized autocorrelation profiles for the $y/\delta \approx 0.5$ and $y/\delta \approx 0.9$ locations show very little variation between the the ZPG and RZPG cases near the correlation origin. This supports the visual analysis made earlier, in which the introduction of surface roughness elements had little impact in relative large-scale turbulence intensity in the upper regions of the boundary layer.

F. Observable Trends

Since this study looked at both favorable pressure gradient and roughness effects on the streamwise-elongated large-scale turbulence structures, as well as the average turbulence statistics for each test case, it is useful to use both sets of information to try and draw conclusions on trends seen between the visual structure intensity, statistical correlation shapes, and the average turbulence statistics for each test condition. Figures 41 & 42 show the average turbulence statistics for the ZPG and RZPG test cases. Comparing this data to the averages presented for the different pressure gradients in Figures 14 and 15, three general trends are visible which may explain the behavior of the relative velocity intensities of the structures, the streamwise correlation of the structures, and the spanwise correlation of the structures.

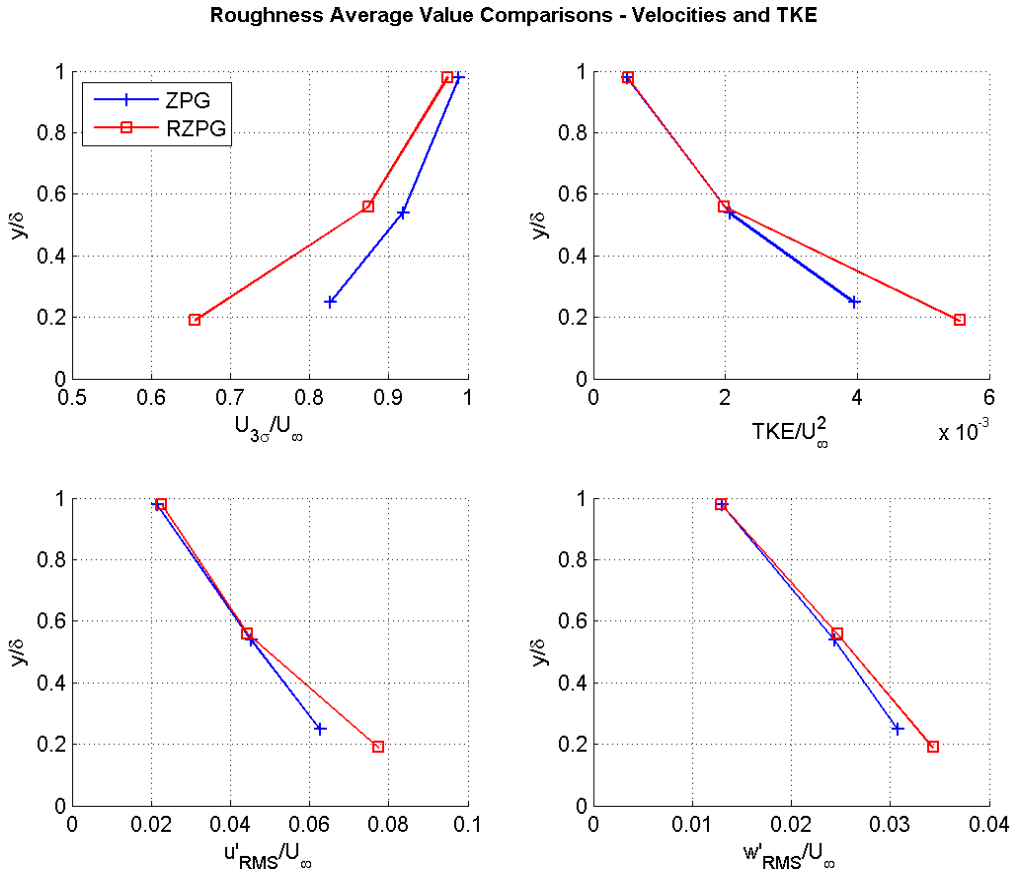

Fig. 41: Average velocity and TKE comparison – ZPG vs. RZPG.

In both the favorable pressure gradient and roughness comparisons, the magnitude difference of the relative high and low velocity regions scales roughly with the u'_{RMS}, w'_{RMS}, TKE, and $\overline{u'w'}$. For each of these values, as their magnitude goes down, so does the relative intensity of the high and low speed structure velocities with respect to the average.

The streamwise correlation width roughly trends with $\overline{u'u'}$ in both cases. As $\overline{u'u'}$ increases, so does the height and width of the R_{ux} profile, at least to some extent. This effect is most clearly seen when comparing the SPG and RZPG cases to the ZPG

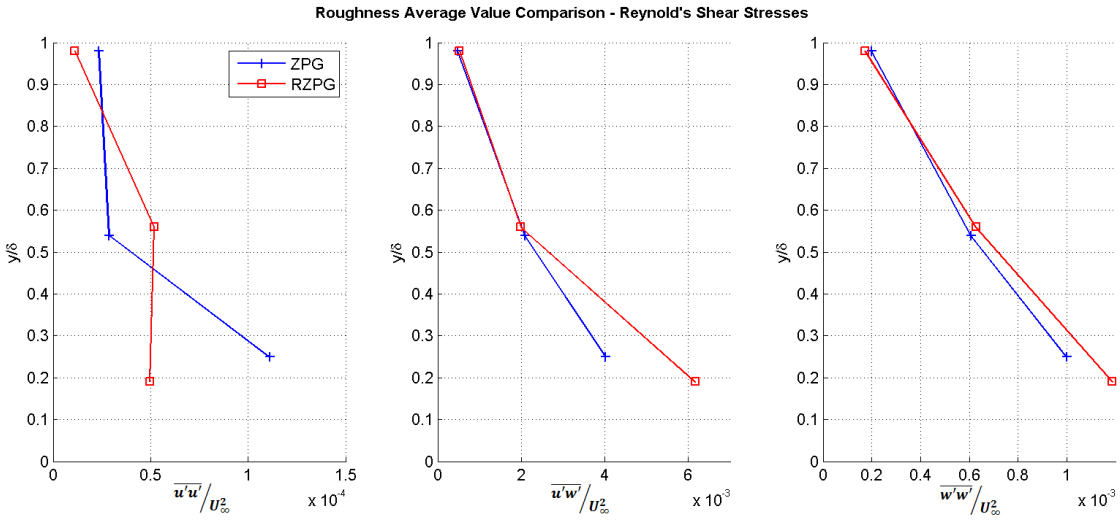

Fig. 42: Reynolds shear stress comparison – ZPG vs. RZPG.

case. When compared to the ZPG at $y/\delta \approx 0.2$, the RZPG case has higher values for ${u'}_{RMS}$, ${w'}_{RMS}$, TKE, $\overline{u'w'}$, & $\overline{w'w'}$, as well as a higher relative turbulence intensity. However, the RZPG still exhibits a lower R_{ux} correlation compared to the ZPG. The only value analyzed in the RZPG turbulence statistics which is lower than its ZPG counterpart is $\overline{u'u'}$. Likewise, in the SPG case where $\overline{u'u'}$ is also lower than in the ZPG, a lower R_{ux} profile results.

Finally, it should be recognized that the spanwise correlation profile tends to trend with the $\overline{w'w'}$ for all cases analyzed. In the favorable pressure gradient comparison, $\overline{w'w'}$ starts out high for the ZPG and WPG, but low for the SPG. As boundary layer height increases, $\overline{w'w'}$ remains almost constant for the SPG, while decreasing in the WPG and ZPG cases. These values trend roughly with the depth of the inversions present in the R_{uz} profile, as shown through Figures 23-25. In the roughness

element comparison, $\overline{w'w'}$ starts off high but at nearly the same value for both the ZPG and RZPG. Both cases show $\overline{w'w'}$ decreasing at the same rate as boundary layer height increases. This behavior is also exhibited in the R_{uz} profile behavior of Figures 36-38. Notice that the R_{uz} profile for the ZPG and RZPG cases remain approximately equivalent while the inversions decrease in magnitude with increased boundary layer height.

These trends clearly need further verification through studies which test other boundary layer heights and pressure gradients. It should further be noted that these trends are only rough estimates of the large scale turbulent properties, and do not exactly predict the large-scale behavior for each location and test case. However, these trends may serve as a general guideline by which the large scale turbulence behavior of a flowfield can be estimated if the u'_{RMS}, w'_{RMS}, TKE, and the Reynolds shear stress components are already known.

CHAPTER V

CONCLUSIONS AND RECOMENDATIONS

A. Summary of Results

Large-scale streamwise elongated structures were found in all test conditions. Visual analysis of the instantaneous velocity fields revealed that these structures were heavily prevalent in the lower boundary layer region of the ZPG and WPG models. The size and distribution of the structures became visually less organized in the SPG and RZPG models, and at the upper boundary layer heights for all three models.

The autocorrelation results added further clarification to the visual analysis. For all boundary layer heights, the ZPG exhibited the highest amount of streamwise correlation, R_{ux}. However, the ZPG model also exhibited the largest variation in spanwise correlation, R_{uz}, with respect to boundary layer height. At the lower and middle boundary layer heights, the ZPG exhibited strong spanwise correlation with deep regularly spaced inversions. However, at the upper boundary layer heights, the spanwise correlation of the ZPG fell off rapidly with no observable inversion. This suggests that the large scale bands became very irregular in spanwise dispersion at the upper layers of the boundary layer.

The strong pressure gradient generally showed the least amount of streamwise correlation, R_{ux}, of the three models tested. However, the SPG also exhibited the least amount of variation in the spanwise correlation profiles, R_{uz}, between different boundary layer heights. This resulted in the weakest relative spanwise correlation at the

lower boundary layer height, but also the strongest amount of spanwise correlation at the upper boundary layer height. The correlation profiles also exhibited a narrowing behavior when moving from the ZPG to the SPG profile in the lower and middle boundary layer regions. This suggests that the introduction of a large favorable pressure gradient shortens the length and narrows the width of the large-scale turbulent structures, while also extending and stabilizing their range and distribution throughout the boundary layer.

The weak pressure gradient displayed behavior in between the other two pressure gradients, in both streamwise and spanwise correlation length and regularity. Although it experienced greater streamwise correlation in the lower and middle boundary layer regions than the SPG case, it experienced slightly less streamwise correlation, R_{ux}, as boundary layer height increased, until it was less correlated than even the SPG at the upper boundary layer height. The WPG experienced more variation in the spanwise correlation, R_{uz}, with boundary layer height than the SPG model, but not as severe of a change as was experienced in the ZPG. However, unlike the SPG, the WPG spanwise correlation profiles were only slightly narrower than the equivalent ZPG profiles. This suggests that the WPG structures were in between the ZPG and SPG structures in streamwise and spanwise size at all 3 boundary layer heights.

Combined, these observations show that the introduction of a favorable pressure gradient shortens and narrows the large-scale streamwise elongated turbulence structures while increasing their range throughout the boundary layer. This results in weaker and more irregular structure of large scale turbulence in the lower regions of the boundary

layer when introduced to a favorable pressure gradient, while also increasing large scale turbulence structure and intensity of the outer regions of the boundary.

The introduction of the roughness elements on the RZPG caused a noticeable visual increase of the relative velocity magnitude of the large scale structures compared to the average velocity when compared to the smooth ZPG model at the lower boundary layer height. It also caused an easily recognizable disturbance of the visual distribution of the streamwise-elongated structures. The autocorrelation results showed a strong decrease in the streamwise correlation, R_{ux}, model at the lower and middle boundary layer heights with the introduction of surface roughness elements. The streamwise correlation at the upper boundary layer region was also reduced, but not as much as was seen at the lower levels. Spanwise correlation was affected much less than the streamwise correlation by the introduction of roughness elements. At the lower boundary layer, a narrowing affect was shown, but the profiles and inversions were the same magnitude. The same effect was noticed at the upper boundary layer location. The middle boundary layer height was slightly different, showing a slight decrease and widening of the spanwise correlation profile, suggesting that the middle and upper layer spanwise structures may not be as well distributed or as prevalent in the roughness element boundary layer profile.

Together, this information suggests that the introduction of surface roughness elements causes a shortening of the streamwise elongated structures, particularly in the lower region, while only slightly narrowing them in the spanwise direction. However, the most drastic effects of the roughness elements were concentrated in the lower and

Table 9: Summary of favorable pressure gradient and roughness element effects.

Change	y/δ	Velocity Difference Intensity	Streamwise Structure Size	Spanwise Structure Size	Spanwise Structure Organization
ZPG ⬇ SPG	0.2	Decrease	10-15% Decrease	15-20% Decrease	10-15% Decrease
	0.5	No Significant Change	10% Decrease	15% Decrease	No Significant Change
	0.9	Increase	5-10% Decrease	5-10% Decrease	10-15% Increase
ZPG ⬇ RZPG	0.2	Increase	15-20% Decrease	10-15% Decrease	No Significant Change
	0.5	No Significant Change	10-15% Decrease	0-5% Increase	5-10% Decrease
	0.9	N/A - y/δ not equivalent	10% Decrease	5-10% Decrease	No Significant Change

middle regions of the boundary layer, with greatly reduced effects in the upper boundary layer.

For all models tested, the streamwise correlation, R_{ux}, exhibited very little change with respect to boundary layer height. Also, in both the favorable pressure gradient and roughness element comparison, the R_{wx} and R_{wz} correlation profiles remained almost completely constant. This suggests a very strong independence of the W velocity correlations on pressure gradient and surface roughness.

Table 9 shows a visual representation of the changes in large scale turbulence intensity, streamwise and spanwise size, and spanwise distribution of large scale turbulence resulting from the introduction of a favorable pressure gradient or roughness elements. In this case, velocity difference intensity refers to the relative velocity magnitude of the high and low speed structures present in each case compared to their respective average velocity. The streamwise and spanwise structure size is based upon the height and width of the R_{ux} and R_{uz} profiles respectively, and the spanwise structure organization refers to the presence and depth of the inversions in the R_{uz} correlation profile.

Certain trends have been identified between the large-scale turbulence structure behavior and the average turbulence statistics of the flowfield. In both the roughness and favorable pressure gradient tests, the relative velocity intensity of the structures scaled roughly with the u'_{RMS}, w'_{RMS}, TKE, and $\overline{u'w'}$. Also, the streamwise and spanwise structure correlation was found to scale roughly with $\overline{u'u'}$ and $\overline{w'w'}$ respectively. While these are only generally observed trends, and not exact, they did hold for all test cases considered in this study.

When compared to the studies done by Ganapathisubramani [11], it was found that the correlation profiles change very little in shape between $M = 2$ and $M = 5$. At the $y/\delta \approx 0.2$ location, the R_{ux} and R_{uz} profiles were nearly identical, with the main difference being a narrowing and deepening of the spanwise correlation profile for the $M = 5$ condition. At the $y/\delta \approx 0.5$ location, the R_{uz} profile was significantly narrower at the higher Mach number. For both locations, R_{wx} and R_{wz} were very similar, with a general narrowing of the profiles for the higher Mach number being the only discernible difference. This suggests that increasing Mach number causes a streamwise narrowing and middle boundary layer height stabilization of the large scale structures, while having very little impact on their streamwise length.

This study has shown that large scale streamwise-turbulence structures are present in a high Mach number flowfield. It also shows that the introduction of a favorable pressure gradient or roughness elements shortens and narrows these structures while shifting their presence and regularity upwards in the boundary layer. Furthermore, the autocorrelation results have shown an almost complete independence of R_{wx} and

R_{wz} on boundary layer profile, roughness, or boundary layer height location, and only a slight dependence of R_{ux} on boundary layer height location. Further comparisons with Ganapathisubramani's work showed only a slight dependence of all four correlation profiles on increasing Mach number, with the main effect being a tightening of the middle boundary layer spanwise structure size and distribution. Finally, several possible trends were identified between the average turbulence statistics and the observed visual and statistical behavior of the large-scale streamwise elongated turbulence structures.

B. Future Work

There are several obvious extensions of this work which would greatly benefit the knowledge of the presence and behavior of large-scale turbulence structures. Perhaps the most important next step is a consideration of the impact of varying adverse pressure gradients on the intensity, size, and distribution of these structures. Studies of the impact of favorable pressure gradient and surface roughness elements at lower Mach number conditions would also be beneficial, especially considering the existence of Ganapathisubramani's $M = 2$ study [11] for comparison. Ultimately, the most beneficial future work may be future attempts to try and validate the trends presented here between large scale structural behavior and the turbulence statistics of the flowfields. If these trends are shown to hold over a large range of conditions, it would allow the prediction of large scale turbulent behavior without the dedicated wide field-of-view studies currently necessary to evaluate them.

Any of these experiments will help to further expand the study of turbulent boundary layers their respond to varying surface shapes and conditions. This knowledge is very important to the design of efficient high speed aerodynamic vehicles, and a clear benefit to the future of transportation, propulsion, and weaponry.

REFERENCES

[1] Whitford, R., "Design for air combat," Jane's, London, Eng; New York, N.Y., 1987.

[2] Office of Naval Research, "U.S. Navy Demonstrates World's Most Powerful EMRG at 10 Megajoules," *Http://www.Navy.Mil/*, January 31, 2008. Accessed February 21, 2013.

[3] Owen, F.K., and Horstmann, C.C., "On the structure of hypersonic turbulent boundary layers," *Journal of Fluid Mechanics,* Vol. 53, No. 04, 1972, pp. 611-636.

[4] Robinson, S.K., "Coherent motions in turbulent boundary layers," *Annual Review of Fluid Mechanics,* Vol. 23, 1991, pp. 601-639.

[5] Panton, R.L., "Self-sustaining mechanisms of wall turbulence," Southampton, UK ; Boston, U.S.A.: Computational Mechanics Pub, Southampton, UK ; Boston, U.S.A., 1997.

[6] Smith, M.W., and Smits, A.J., "Visualization of the structure of supersonic turbulent boundary layers," *Experiments in Fluids,* Vol. 18, No. 4, 1995, pp. 288-302.

[7] Head, M.R., and Bandyopadhyay, P., "New aspects of turbulent boundary-layer structure," *Journal of Fluid Mechanics,* Vol. 107, No. -1, 1981, pp. 297-338.

[8] Smith, M., Smits, A., and Miles, R., "Compressible boundary layer density cross section by uv rayleigh scattering," *Optics Letters,* Vol. 14, No. 17, 1989, pp. 916-918.

[9] Ganapathisubramani, B., Longmire, E.K., and Marusic, I., "Characteristics of vortex packets in turbulent boundary layers," *Journal of Fluid Mechanics,* Vol. 478, 2003, pp. 35-46.

[10] Tomkins, C.D., and Adrian, R.J., "Spanwise structure and scale growth in turbulent boundary layers," *Journal of Fluid Mechanics,* Vol. 490, 2003, pp. 37-74.

[11] Ganapathisubramani, B., Clemens, N.T., and Dolling, D.S., "Large-scale motions in a supersonic turbulent boundary layer," *Journal of Fluid Mechanics,* Vol. 556, 2006, pp. 271-312.

[12] Humble, R.A., Elsinga, G.E., Scarano, F., and Van Oudheusden, B.W., "Three-dimensional instantaneous structure of a shock wave/turbulent boundary layer interaction," *Journal of Fluid Mechanics,* Vol. 622, 2009, pp. 33-62.

[13] Ringuette, M., Minwei, W., and Martin, M.P., "Coherent structures in direct numerical simulation of turbulent boundary layers at Mach 3," *Journal of Fluid Mechanics,* Vol. 594, 2008, pp. 59-69.

[14] Bradshaw, P., "The effect of mean compression or dilatation on the turbulence structure of supersonic boundary layers," *Journal of Fluid Mechanics,* Vol. 63, No. 03, 1974, pp. 449-464.

[15] Spina, E., Smits, A., and Robinson, S., "The Physics of Supersonic Turbulent Boundary Layers," *Annual Review of Fluid Mechanics,* Vol. 26, 1994, pp. 287-319.

[16] Tichenor, N.R., "*Characterization of the Influence of a Favorable Pressure Gradient on the Basic Structure of a Mach 5.0 High Reynolds Number Supersonic Turbulent Boundary Layer*," *Department of Aerospace Engineering, Texas A&M University,* 2010.

[17] Tichenor, N.R., Humble, R.A., and Bowersox, R.D.W., "Response of a Hypersonic Turbulent Boundary Layer to Favorable Pressure Gradients," *Journal of Fluid Mechanics,* Vol. (submitted for review), 2012.

[18] Peltier, S.J., Humble, R.A., and Bowersox, R.D.W., "Response of a Hypersonic Turbulent Boundary Layer to Local and Global Mechanical Distortions," AIAA Paper 2011-680.

[19] Peltier, S.J., Humble, R.A., and Bowersox, R.D.W., "The Influence of Favorable Pressure Gradients upon the Coherent Motions in a Mach 5 Turbulent Boundary Layer," AIAA Paper, 2012-3060.

[20] Humble, R., Peltier, S., and Bowersox, R., "Visualization of the structural response of a hypersonic turbulent boundary layer to convex curvature," *Physics of Fluids,* Vol. 24, No. 10, 2012, pp. 103-106.

[21] Tilmann, C.P., Bowersox, R.D.W., and Buter, T.A., "On the Design and Construction of an Academic Mach 5 Wind Tunnel," AIAA Paper 1999-0800.

[22] Ekoto, I.W., Bowersox, R., Beutner, T., "Supersonic boundary layers with periodic surface roughness," *AIAA Journal,* Vol. 46, No. 2, 2008, pp. 486-497.

[23] Ekoto, I., "Response of supersonic turbulent boundary layers to local and global mechanical distortions," *Journal of Fluid Mechanics,* Vol. 630, 2009, pp. 225-265.

[24] Peltier, S.J., Humble, R.A., and Bowersox, R.D.W., "PIV of a Mach 5 turbulent boundary layer over diamond roughness elements," AIAA Paper 2012-3061.

[25] German Aerospace Center - DLR, "Institute of Aerodynamics and Flow Technology - Experimental Methods - Principle PIV Setup," *Http://www.dlr.de/*, Accessed February 22, 2013.

[26] Ragni, D., Schrijer, F., Oudeheusden, B.W.V., "Particle tracer response across shocks measured by PIV," *Experiments in Fluids,* Vol. 50, No. 1, 2011, pp. 53-64.

[27] Benedict, L.H. and Gould, R.D., "Towards better uncertainty estimates for turbulence statistics," *Experiments in Fluids,* Vol. 22, No. 2, 1996, pp. 129-136.